

RESEARCH ARTICLE

Remodeling of organelles and microtubules during spermiogenesis in the liverwort *Marchantia polymorpha*

Naoki Minamino¹, Takuya Norizuki¹, Shoji Mano^{2,3}, Kazuo Ebine^{1,3} and Takashi Ueda^{1,3,*}

ABSTRACT

Gametogenesis is an essential event for sexual reproduction in various organisms. Bryophytes employ motile sperm (spermatozooids) as male gametes, which locomote to the egg cells to accomplish fertilization. The spermatozooids of bryophytes harbor distinctive morphological characteristics, including a cell body with a helical shape and two flagella. During spermiogenesis, the shape and cellular contents of the spermatids are dynamically reorganized. However, the reorganization patterns of each organelle remain obscure. In this study, we classified the developmental processes during spermiogenesis in the liverwort *Marchantia polymorpha* according to changes in cellular and nuclear shapes and flagellar development. We then examined the remodeling of microtubules and the reorganization of endomembrane organelles. The results indicated that the state of glutamylation of tubulin changes during formation of the flagella and spline. We also found that the plasma membrane and endomembrane organelles are drastically reorganized in a precisely regulated manner, which involves the functions of endosomal sorting complexes required for transport (ESCRT) machineries in endocytic and vacuolar transport. These findings are expected to provide useful indices to classify developmental and subcellular processes of spermiogenesis in bryophytes.

KEY WORDS: Spermiogenesis, Microtubule, Organelle, ESCRT, *Marchantia polymorpha*

INTRODUCTION

Sexual reproduction, one of the most crucial events in the life cycle of multicellular organisms, is necessary for genetic variation and thus adaptation to environments. To accomplish sexual reproduction, specifically in oogamy, reproductive cells (generally classified into male and female gametes) are generated through precisely regulated differentiation and maturation processes. A majority of seed plants generate non-motile male gametes, which are transported to the egg cells via pollen tubes for fertilization. Conversely, some species in streptophyte algae as well as bryophytes, lycophytes, ferns and some groups of gymnosperms, such as ginkgo and cycads, generate motile sperm cells (spermatozooids) as male gametes, which harbor two or more

motile flagella and move towards egg cells in water to accomplish fertilization. Gametogenesis in angiosperms has been intensively studied using several species including *Arabidopsis thaliana*, and its mechanisms are well documented at the genetic and molecular levels (Berger and Twell, 2011; Hackenberg and Twell, 2019; Russell and Jones, 2015; Twell, 2011). Conversely, molecular genetic studies of gametogenesis in basal land plants producing spermatozooids have only recently begun, using a few bryophyte models such as *Physcomitrium patens* and *Marchantia polymorpha* (Higo et al., 2018; Koi et al., 2016; Koshimizu et al., 2018; Minamino et al., 2017; Sanchez-Vera et al., 2017).

Spermatozooids of bryophytes have distinctive morphological characteristics, some of which are also shared with spermatozooids of other plant lineages. The cell body exhibits a helical shape and consists mostly of an elongated nucleus. The anterior region of the cell body contains one mitochondrion, which is associated with the multilayered structure (MLS), a characteristic of plant spermatids. The uppermost layer of the MLS (opposite the mitochondrion) is a bundle of microtubules, termed the spline, which extends along the helical nucleus through the cell body. Two flagella elongate from two basal bodies, which are attached to the spline of the MLS. The posterior side of the cell body contains the other mitochondrion and a plastid, and other cytoplasmic components are not appreciably observed in mature spermatozooids (Fig. 1A; Shimamura, 2016; Renzaglia and Garbary, 2001). During the transformation from spermatids to spermatozooids, which is termed spermiogenesis, the cell shape and cellular contents of spermatids are drastically reorganized. The MLS and flagella are formed *de novo* during spermiogenesis, a process that has been investigated mainly using electron microscopy (Carothers and Kreitner, 1967, 1968; Kreitner, 1977a; Kreitner and Carothers, 1976; Renzaglia and Duckett, 1987; Renzaglia and Garbary, 2001). It is expected that most of the cytoplasm, including various organelles other than the nucleus, the anterior and posterior mitochondria, and a plastid, is eliminated during spermiogenesis. However, when and how organelles are removed from spermatids during spermiogenesis remains unknown, mainly due to the lack of proper methods to observe spatiotemporal organelle dynamics during plant spermiogenesis.

M. polymorpha is a model of liverworts, a group of bryophytes for which the genomic information is available (Bowman et al., 2017; Montgomery et al., 2020), and for which various tools for molecular genetic analyses have been established (Kohchi et al., 2021). Transcriptome data and a wide variety of organelle markers have also been developed for *M. polymorpha* (Bowman et al., 2017; Higo et al., 2016; Kanazawa et al., 2016; Minamino et al., 2017, 2018). By employing this relatively new model plant for analyzing the cellular dynamics during plant spermiogenesis, we have previously reported that subcellular localizations of some organelle markers drastically change and that degradation events, such as endocytic and autophagic degradation, are highly activated in the spermatogenous tissue (Minamino et al., 2017). However, the

¹Division of Cellular Dynamics, National Institute for Basic Biology, Nishigonaka 38, Myodaiji, Okazaki, Aichi, 444-8585, Japan. ²Laboratory of Organelle Regulation, National Institute for Basic Biology, Nishigonaka 38, Myodaiji, Okazaki, Aichi, 444-8585, Japan. ³Department of Basic Biology, SOKENDAI (The Graduate University for Advanced Studies), Nishigonaka 38, Myodaiji, Okazaki, Aichi, 444-8585, Japan.

*Author for correspondence (tueda@nibb.ac.jp)

DOI: N.M., 0000-0003-4600-0084; T.N., 0000-0002-0781-9671; S.M., 0000-0003-1323-3308; K.E., 0000-0003-3020-7208; T.U., 0000-0002-5190-892X

Handling Editor: Ykä Helariutta

Received 18 May 2022; Accepted 23 June 2022

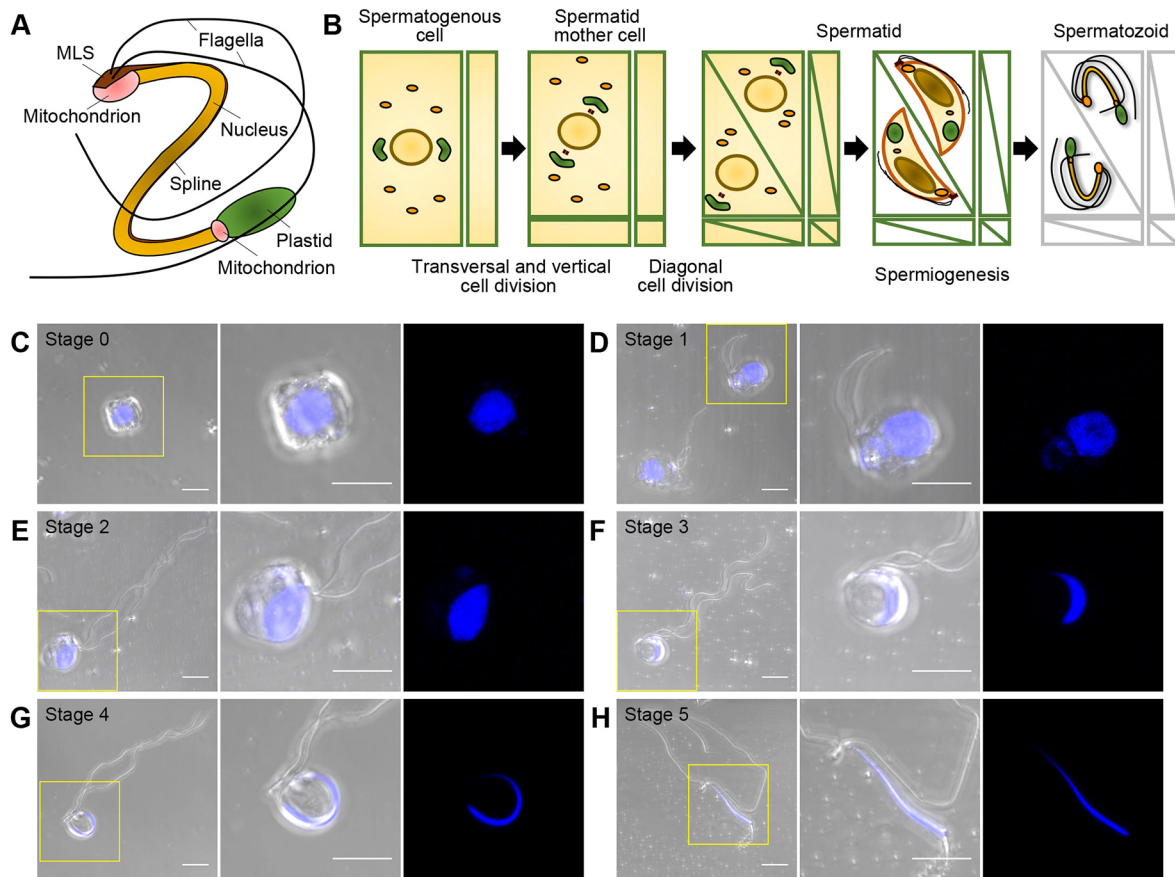


Fig. 1. Developmental stages of spermiogenesis in *M. polymorpha*. (A,B) Schematic illustration of spermatozoids (A) and male gamete development (B). (C-H) Maximum-intensity projection images of spermatids and a spermatozoid stained with Hoechst 33342. Left panels, merged images of differential interference contrast (DIC) and fluorescent images; middle panels, higher magnification images of the boxed areas in the left panels; right panels, fluorescent images of nuclei in middle panels. The blue pseudo-color indicates fluorescence from Hoechst 33342. Images are representative of 30 (C), 36 (D), 36 (E), 26 (F), 29 (G) and 27 (H) cells. Scale bars: 5 μ m.

temporal resolution of this study was not sufficient owing to the lack of defined developmental stages; thus, the contributions of these degradation events to spermiogenesis in *M. polymorpha* remain unclear.

The endosomal sorting complexes required for transport (ESCRTs) mediate the degradation of membrane proteins, including plasma membrane (PM) proteins, by forming intraluminal vesicles (ILVs) in the multivesicular endosomes (MVEs) and sorting ubiquitinated membrane proteins to be degraded into ILVs. MVEs then fuse with the vacuole and the ILVs are released into the vacuolar lumen to be degraded by hydrolytic enzymes stored in the vacuole (Isono, 2021). Because many PM and organelle proteins are degraded during spermiogenesis (Minamino et al., 2017), ESCRTs could play a crucial role in spermiogenesis in *M. polymorpha*.

To address these possibilities in this study, we first classified the developmental processes of spermiogenesis in *M. polymorpha* according to cellular and nuclear morphology and flagellar formation. We then examined microtubule organization in each developmental stage during spermiogenesis and observed when and how each organelle/organelle protein is degraded during spermiogenesis. We then examined whether ESCRT activity is required for spermiogenesis in *M. polymorpha* by perturbing ESCRT function. The results of these experiments demonstrate a drastic but highly organized rearrangement of cellular components during spermiogenesis in *M. polymorpha*, which is at least partly

mediated by ESCRTs. This work also provides a useful index for classification of the developmental stages of spermatids undergoing spermiogenesis in bryophytes.

RESULTS

Determining the developmental stages of spermiogenesis in *M. polymorpha*

An antheridium of *M. polymorpha* consists of outer jacket cells and inner reproductive cells. Spermatogenous cells proliferate by continuous transverse and vertical cell division, and the resultant spermatid mother cells divide diagonally to generate spermatids (Fig. 1B, Ikeno, 1903; Shimamura, 2016). Spermatids then transform into mature spermatozoids through spermiogenesis. Spermiogenesis of *M. polymorpha* comprises dynamic cellular reorganization events, including condensation and elongation of the nucleus, *de novo* synthesis of the locomotory apparatus and elimination of the cytoplasm (Fig. 1B; Shimamura, 2016). Based on the morphology of the cell body, the nuclear shape observed with Hoechst 33342 and the formation of flagella, we first attempted to classify spermatid cells undergoing spermiogenesis, which were fixed with paraformaldehyde and separated from each other by treating with cell-wall-digesting enzymes, into 1+5 developmental stages (Fig. 1C-H). The cells harboring the spherical nucleus without visible flagella were classified as stage 0. These cells presumably contained spermatogenous cells, spermatid mother cells and early-stage spermatids, which were not distinguishable from

each other based on their morphology after cell-wall digestion (Fig. 1C). At stage 1, protruding or elongating flagella were observed, whereas the nucleus remained spherical (Fig. 1D). A change in the nuclear shape was detected from stage 2. At this stage, spermatids were equipped with fully elongated flagella and the projection of the anterior side of the nucleus was also visible (Fig. 1E). At stage 3, the nucleus became crescent shaped (Fig. 1F) and a cylindrical nucleus was observed at stage 4 (Fig. 1G). Mature spermatozooids were defined as stage 5 (Fig. 1H).

Microtubule organization during spermiogenesis in *M. polymorpha*

The spermatozoid of *M. polymorpha* comprises two distinctive microtubule-containing structures: the flagella and the spline. To examine how microtubules are organized during spermiogenesis to form these structures, we performed immunostaining of tubulin in spermatids at distinct developmental stages. In addition to immunostaining using an anti- α -tubulin antibody, we also performed staining with an anti-polyglutamate (polyE) antibody, which recognizes carboxyl (C)-terminally located linear α -glutamate chains of four or more glutamate residues. This method was chosen knowing that post-translational modifications, including glutamylation, are detected in persistent microtubules in the axoneme in animals and in *Chlamydomonas reinhardtii* (Janke and Magiera, 2020; Wloga et al., 2017). In some cells at stage 0, fibrous structures stained only with the anti- α -tubulin antibody were observed near the cell surface (Fig. 2A). In other cells, rod-like forming flagella, which had not yet protruded from the cell body, were stained by both the anti- α -tubulin and anti-polyE antibodies (Fig. 2B). In stage 1 spermatids, elongating flagella were observed, stained by both antibodies (Fig. 2C). Notably, microtubule fibers

extending radially from or toward the basal region of the forming flagella were frequently observed at stages 0 and 1 (Fig. 2B,C). The radial fibers were not observed in stage 2 spermatids, whereas the spline microtubules were stained by the anti- α -tubulin antibody in stage 2 and 3 spermatids (Fig. 2D,E). The radial structure and spline were not stained by the anti-polyE antibody (Fig. 2B-E). Intriguingly, the signal intensity from α -tubulin on flagella became weaker except for that in the distal-most regions at stages 2 to 3; however, the signal from polyE was uniformly detected at the corresponding regions (Fig. 2D,E). Similar results were also obtained when we used another anti- α -tubulin antibody and an anti- β -tubulin antibody (Fig. S2A-D). At stage 4, the polyE signal was detected on flagella, but α -tubulin was not detected on either the flagella or the spline (Fig. 2F). At stage 5 (mature spermatozooids), the α -tubulin signal was detected again on both the flagella and the spline. The polyE signal was also detected on the flagella and the spline, although the intensity of the signal from the spline was weak compared with that from the flagella (Fig. 2G; Fig. S1). We then performed immunoblotting to examine whether the anti-polyE antibody recognized the same tubulin population as anti- α - and anti- β -tubulin antibodies. The anti- α - and β -tubulin antibodies detected tubulin molecules at approximately 50 kDa, whereas the anti-polyE antibody reacted with the product at approximately 58 kDa in cell lysates prepared from antheridia (Fig. S3). The anti- α - and β -tubulin antibodies did not react with the 58 kDa product detected with the anti-polyE antibody, and vice versa. Given that the shift of the molecular weight would reflect the covalently added polyglutamate chain, as reported in previous studies (Kubo et al., 2010, 2014; Vu et al., 2016), and that both the epitopes of the anti-tubulin antibodies used in this study and polyglutamylation sites are mapped to the C-terminal region of tubulin, the anti-tubulin antibodies and the anti-

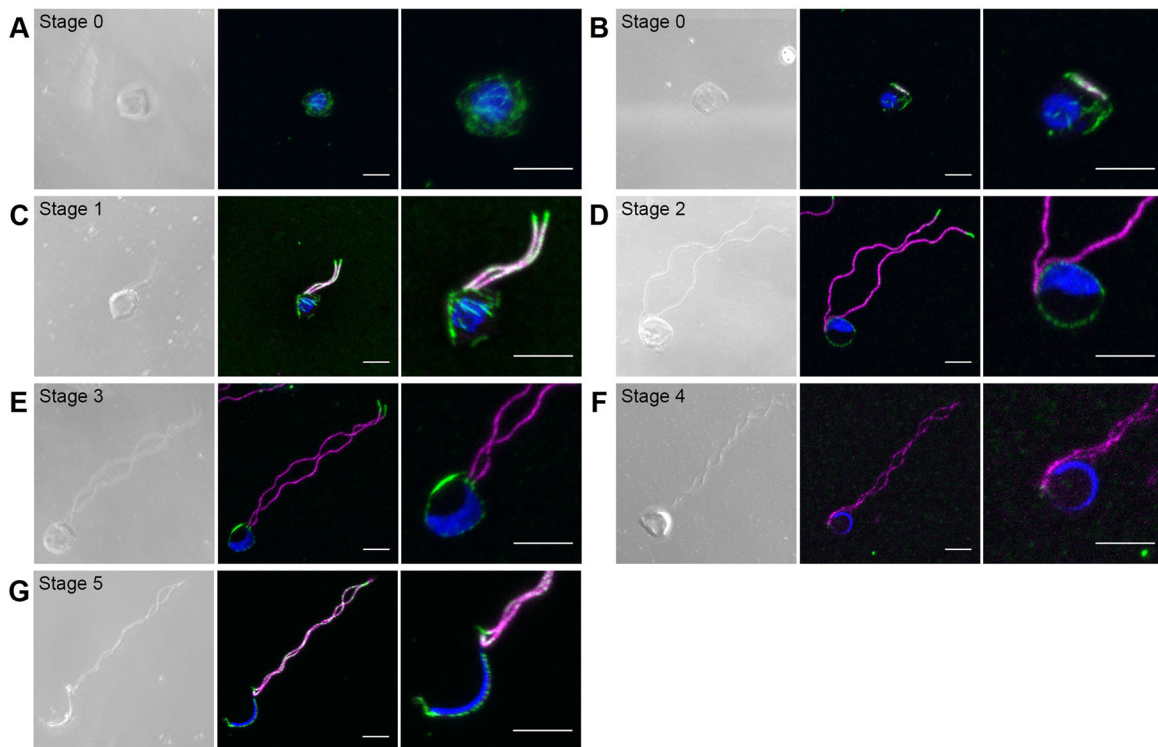


Fig. 2. Microtubule dynamics during spermatogenesis. (A-G) Maximum-intensity projection images of spermatids and a spermatozoid immunostained with anti- α -tubulin (DM1A) and anti-polyE antibodies. Left panels, DIC images; middle panels, fluorescent images; right panels, higher magnification images of middle panels. Green, magenta and blue pseudo-colors indicate fluorescence from Alexa Fluor 488 (α -tubulin), Alexa Fluor 594 (polyE) and Hoechst 33342, respectively. Images are representative of 13 (A), 6 (B), 15 (C), 13 (D), 9 (E), 8 (F) and 11 (G) cells. Scale bars: 5 μ m.

polyE antibody react exclusively with distinct populations of tubulin molecules. Thus, our results strongly suggest that tubulin molecules in the axoneme and spline undergo a progressive alteration in post-translational modifications during spermiogenesis.

Selection of promoters for the expression of organelle markers in spermatogenous tissue of *M. polymorpha*

With the goal of observing the behavior of endomembrane organelles during spermiogenesis without interference from surrounding tissues, we expressed organelle markers under the regulation of promoters predominantly active in spermatids. We selected three candidate genes that have been reported to be expressed strongly during spermiogenesis in *M. polymorpha*. MpDUO1 is a MYB transcription factor, which is required for spermatozoid differentiation of *M. polymorpha* (Higo et al., 2018). MpCEN1 is a homolog of CENTRIN, which is essential for the formation of the locomotory apparatus in the fern *Marsilea vestita*, and is strongly expressed in spermatogenous tissue independently of MpDUO1 in *M. polymorpha* (Higo et al., 2018; Klink and Wolniak, 2001). IFT52 is one of the components of the intraflagellar transport complex essential for flagellar formation in *C. reinhardtii* (Brazelton et al., 2001; Deane et al., 2001) and its homolog MpIFT52 in *M. polymorpha* is abundantly expressed in antheridiophores, according to the transcriptome data deposited in MarpolBase (<https://marchantia.info/>). Transgenic lines expressing the fluorescent protein Citrine driven by the promoters of these genes exhibited strong expression in spermatogenous tissue (Fig. S4A–C), suggesting that these promoters may be useful for the expression of organelle markers during spermatogenesis. We thus used these promoters for further experiments in this study (Fig. S4D).

Reorganization of vacuoles during spermiogenesis in *M. polymorpha*

We previously reported that PM proteins and several endomembrane organelle proteins are transported into the luminal

space of spherical vacuoles to be degraded during spermiogenesis (Minamino et al., 2017). However, it remains unknown when the vacuole transforms to a spherical shape, and it also remains unclear how transport of organelle proteins to the vacuole is organized. To determine this, we first examined alteration of vacuolar morphology during spermiogenesis using a vacuole-residing soluble *N*-ethylmaleimide-sensitive factor attachment protein receptor (SNARE), MpVAMP71 (Kanazawa et al., 2016), tagged with monomeric Citrine (mCitrine-MpVAMP71), expressed under the regulation of the MpDUO1 promoter. In cells at stages 0 and 1, small and fragmented vacuoles with intricate morphology were observed around the nucleus (Fig. 3A,B). However, only one spherical vacuole was observed in each spermatid at stage 2 (Fig. 3C), which persisted through stages 3 and 4 (Fig. 3D,E). In mature spermatozooids (stage 5), compartments with mCitrine-MpVAMP71 were not detected (Fig. 3F). Thus, vacuoles drastically change their morphology and number before stage 2 to form a spherical vacuole, which is eliminated after stage 4 to accomplish spermiogenesis.

Dynamic reorganization of the plasma and endo-membranes during spermiogenesis

A PM-resident SNARE, MpSYP12A (Kanazawa et al., 2016), tagged with mCitrine (mCitrine-MpSYP12A), was shown to be removed from the PM during spermiogenesis, suggesting that drastic remodeling also takes place in the PM in spermatids undergoing spermiogenesis (Minamino et al., 2017). To elucidate the precise timing of this event, we observed spermatids expressing mCitrine-MpSYP12A at each developmental stage. At stage 0, mCitrine-MpSYP12A was detected on the PM and in punctate compartments (Fig. 4A,B). At stage 1, the fluorescent signal on the PM was diminished and bright fluorescence was observed in punctate compartments (Fig. 4C), which probably represent the small vacuoles observed in spermatids at stage 1 (Fig. 3B). The signal from mCitrine was still detectable in the lumen of the larger spherical vacuole in some spermatids at stage 2 (Fig. 4D), whereas

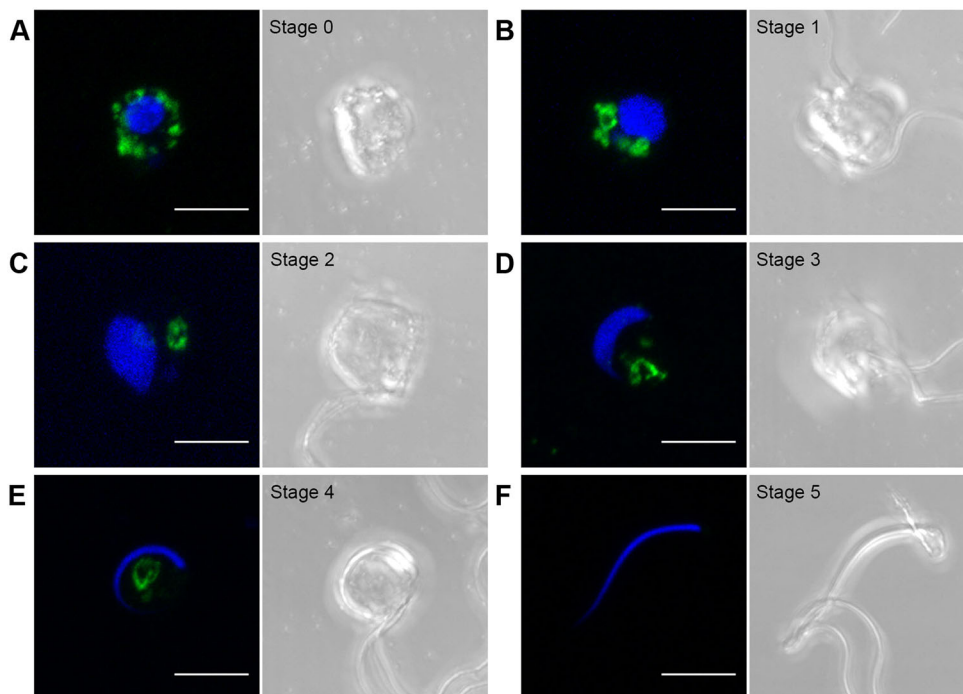


Fig. 3. Changes in vacuolar morphology during spermiogenesis. (A–F) Maximum-intensity projection images of spermatids and a spermatozoid expressing mCitrine-MpVAMP71 driven by the MpDUO1 promoter. Left panels, fluorescent images; right panels, DIC images. Green and blue pseudo-colors indicate fluorescence from mCitrine and Hoechst 33342, respectively. Images are representative of 19 (A), 15 (B), 22 (C), 18 (D), 17 (E) and 18 (F) cells. Scale bars: 5 μ m.

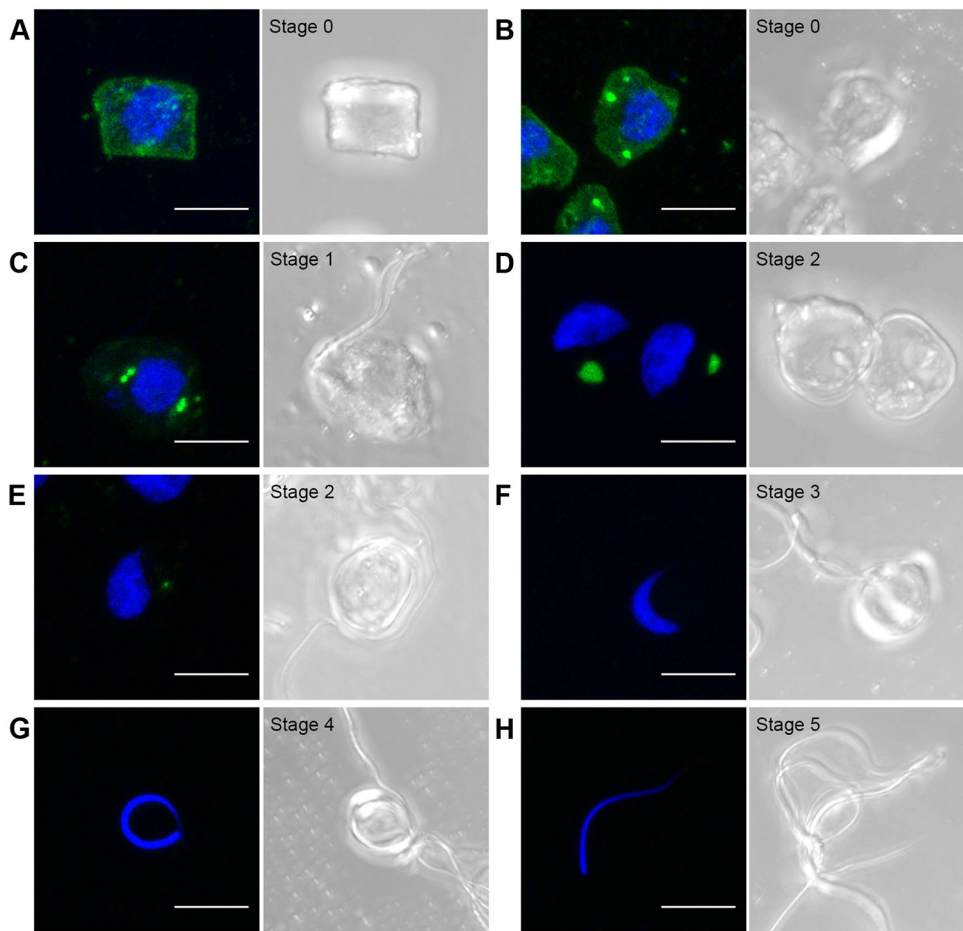


Fig. 4. Remodeling of the plasma membrane during spermiogenesis. (A-H) Maximum-intensity projection images of spermatids and a spermatozoid expressing mCitrine-MpSYP12A driven by the MpDUO1 promoter. Left panels, fluorescence images; right panels, DIC images. Green and blue pseudo-colors indicate fluorescence from mCitrine and Hoechst 33342, respectively. Images are representative of 13 (stage 0), 15 (stage 1), 15 (stage 2), 13 (stage 3), 9 (stage 4) and 13 (stage 5) cells. Scale bars: 5 μ m.

only faint or almost no fluorescence was detected in the majority of spermatids at this stage (Fig. 4E). We did not detect any fluorescence after stage 3 (Fig. 4F-H). These results indicate that endocytosis was highly activated between stages 0 and 1, and that PM proteins including MpSYP12A were removed almost completely from the PM and degraded in the vacuole during stage 2, suggesting rapid remodeling of the PM at early stages during spermiogenesis.

The Golgi apparatus also exhibited drastic changes in morphology and number during spermiogenesis. We observed the Golgi apparatus during spermiogenesis using the Venus-fused transmembrane domain of sialyltransferase (ST) derived from rat, which is localized to the Golgi apparatus in *M. polymorpha* (Kanazawa et al., 2016). Although several discrete Golgi apparatuses were observed at stage 0, only one Golgi apparatus, which was enlarged compared with the Golgi apparatus at earlier stages, was observed in cells at stage 2 (Fig. 5A-C,G,H). Appearance of the large Golgi apparatus in spermatids undergoing spermiogenesis has also been reported in electron microscopic observations of another liverwort, *Blasia pusilla* (Renzaglia and Duckett, 1987). The fluorescence from ST-Venus was decreased in spermatids at stage 3 and was not detectable in cells at stages 4 and 5 (Fig. 5D-F). We also observed similar behavior of the Golgi apparatus using other Golgi markers, mCitrine-fused MpGOS11 and MpSFT1 (Kanazawa et al., 2016); these markers were hardly detected at stage 3 (Fig. S5). Thus, one large Golgi apparatus is formed during the early stages of spermiogenesis, and resident proteins are degraded during later stages.

We then observed changes in the endoplasmic reticulum (ER). As an ER membrane marker, we used mCitrine-fused MpSEC22 (mCitrine-MpSEC22; Kanazawa et al., 2016). We also monitored the soluble ER protein marker SP-mCitrine-HDEL, which consists of mCitrine tagged with the signal peptide (SP) at its N-terminus and four amino acids (His-Asp-Glu-Leu) sufficient for ER localization at the C-terminus (Mano et al., 2018). These ER markers illuminated the nuclear envelope (NE) and the ER until stage 2 (Fig. 6A-F). Intriguingly, the fluorescence at the NE was hardly detected at stage 3, whereas the signal on the ER remained detectable at this stage (Fig. 6G-I), suggesting distinct regulation of remodeling between the NE and ER during spermiogenesis. Furthermore, we found that these two ER markers behaved distinctly at later stages; SP-mCitrine-HDEL remained at the anterior region of spermatozooids and a faint signal was also detected in other regions (Fig. 6L), whereas the signal from mCitrine-MpSEC22 was not detected in spermatozooids (Fig. 6K). Thus, remodeling of the ER also takes place in a highly organized manner, with distinct temporal regulation depending on domains and proteins.

ESCRTs play crucial roles in spermiogenesis

Given that the PM and organelle proteins are rapidly degraded during spermiogenesis, we speculated that ESCRT-mediated degradation could be involved in spermatozoid development. Knockout mutations of ESCRT subunits and accessory proteins can severely affect the viability and/or growth of *A. thaliana* and *Oryza sativa* (Gao et al., 2014; Isono et al., 2010; Katsiarimpa et al.,

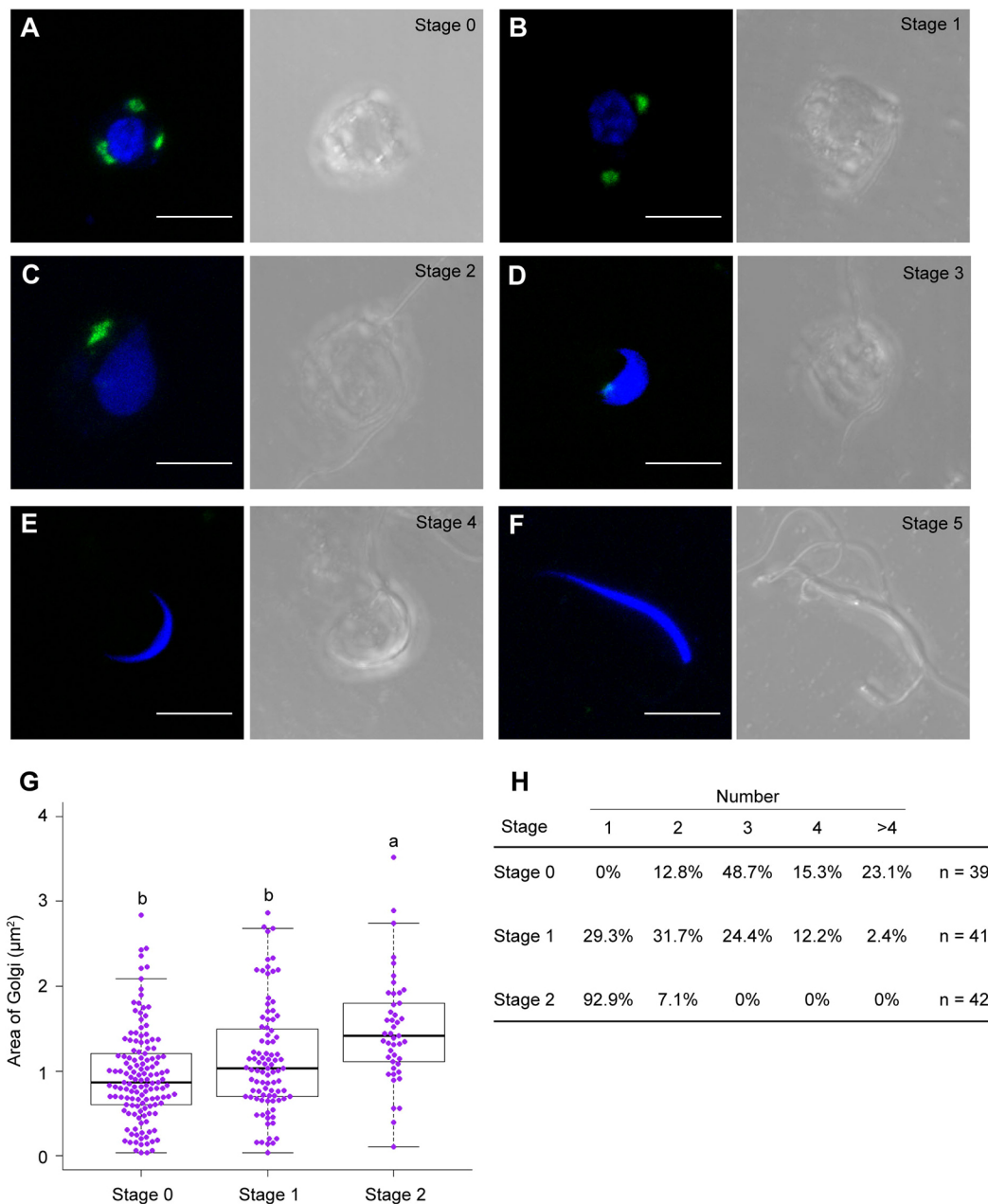


Fig. 5. Reorganization of the Golgi apparatus during spermiogenesis. (A-F) Maximum-intensity projection images of spermatids and a spermatozoid expressing ST-Venus driven by the *MpDUO1* promoter. Left panels, fluorescence images; right panels, DIC images. Green and blue pseudo-colors indicate fluorescence from mCitrine and Hoechst 33342, respectively. Images are representative of 39 (A), 41 (B), 42 (C), 40 (D), 5 (E) and 24 (F) cells from two independent lines. Scale bars: 5 μm . (G) Quantification of the size of the Golgi apparatus labeled by ST-Venus. $n=137$ (stage 0), 91 (stage 1) and 45 puncta (stage 2). The boxes and solid lines in the boxes indicate the first and third quartiles and the median values, respectively. The upper and lower whiskers are drawn at the greatest value smaller than $1.5\times$ interquartile ranges above the third quartile and the smallest value greater than $1.5\times$ interquartile ranges below the first quartile, respectively. Different letters denote significant differences based on Tukey's test ($P<0.05$). (H) Quantification of the number of the Golgi apparatus labeled by ST-Venus. The difference in the number of the Golgi apparatus between stages was statistically significant based on Tukey's test ($P<0.05$). See also Fig. S5.

2011; Kolb et al., 2015; Nagel et al., 2017; Spitzer et al., 2009; Zhang et al., 2013); therefore, a knockout strategy with loss-of-function mutants of ESCRT subunits would not be practical to analyze the role of ESCRTs in *M. polymorpha* spermiogenesis. One of the multi-subunit protein complexes of ESCRTs, ESCRT-III, generally consists of four evolutionarily conserved proteins: VPS20, SNF7, VPS2 and VPS24. ESCRT-III mediates the scission of ILVs from the limiting membrane of the MVE (Isono, 2021). Overexpression of the ESCRT-III subunit SNF7 fused with fluorescent proteins at the C-terminus was reported to confer a

dominant-negative effect and inhibited the degradation of PM proteins in various organisms, including *A. thaliana* (Cai et al., 2014; Teis et al., 2008; Teis et al., 2010). To verify our hypothesis, we thus employed this strategy to attenuate the activity of ESCRTs during spermiogenesis in *M. polymorpha*. We generated transgenic lines expressing C-terminal mGFP-fused *MpSNF7a*, which is homologous to *A. thaliana* SNF7 (Fig. S6A), under regulation of the *MpDUO1* promoter. *MpSNF7a*-mGFP formed large fluorescent structures in the cytoplasm of spermatids reminiscent of the class E compartment, which is an aberrant endosomal structure formed by

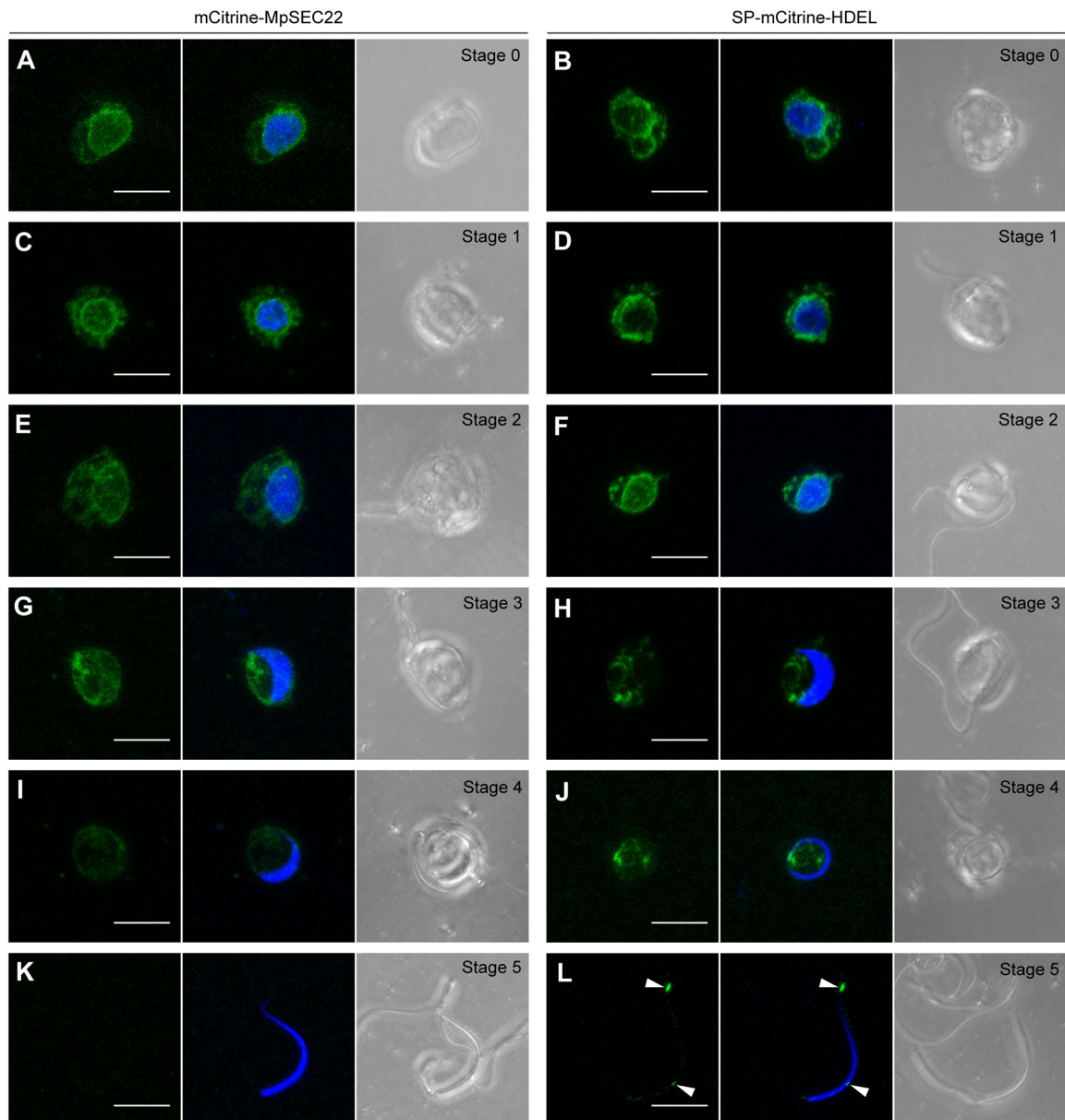


Fig. 6. Reorganization of the ER and the nuclear envelope during spermiogenesis. Maximum-intensity projection images of spermatids and spermatozooids expressing mCitrine-MpSEC22 driven by the MpDUO1 promoter (A,C,E,G,I,K) or SP-mCitrine-HDEL driven by the MpEF1 α promoter (B,D,F,H,J,L). Arrowheads indicate SP-mCitrine-HDEL remaining in spermatozooids. Left panels, fluorescence images of mCitrine; middle panel, merged images of mCitrine and Hoechst 33342; right panels, DIC images. Green and blue pseudo-colors indicate fluorescence from mCitrine and Hoechst 33342, respectively. Each image is representative of at least 15 cells from two independent lines. Scale bars: 5 μ m.

dysfunction of ESCRTs in yeast and mammalian cells (Fig. 7A) (Howard et al., 2001; Raymond et al., 1992; Reider et al., 1996). The plants expressing MpSNF7a-mGFP rarely released spermatozooids into water, and the spermatozooids we could observe were almost completely immotile under a dark-field microscope, although they were equipped with flagella (Movies 1 and 2). Hoechst 33342 staining showed that the nuclei of MpSNF7a-mGFP spermatozooids were not fully elongated compared with those of control spermatozooids that exhibited a cylindrically elongated shape (Fig. 7C,D). The abnormal shape of the nuclei of MpSNF7a-mGFP spermatozooids was confirmed by quantification of the circularity of the nucleus; the circularity of nuclei in MpSNF7a-mGFP spermatozooids was significantly higher than that of control nuclei (Fig. 7F). Similar effects were also observed by overexpressing

another dominant-negative type of ESCRT-III subunit, mGFP-tagged MpVPS24 with deletion of the C-terminal region (MpVPS24¹⁻¹⁵²), as reported in *A. thaliana* (Cai et al., 2014), confirming that these effects were attributed to the dysfunction of ESCRT-III (Fig. 7B,E,F; Fig. S6; Movie 3).

We then examined whether PM protein degradation is altered during spermiogenesis in MpSNF7a-mGFP and MpVPS24¹⁻¹⁵²-mGFP plants by introducing mCitrine-MpSYP12A driven by its own promoter. We also generated transgenic plants expressing mGFP and mCitrine-MpSYP12A as a negative control. In the control spermatids, the mCitrine-MpSYP12A signal was detected in the spherical vacuole at the later stage of spermiogenesis, consistent with our previous observation (Fig. S6B; Minamino et al., 2017). However, no mCitrine signal was detected in spherical vacuoles or

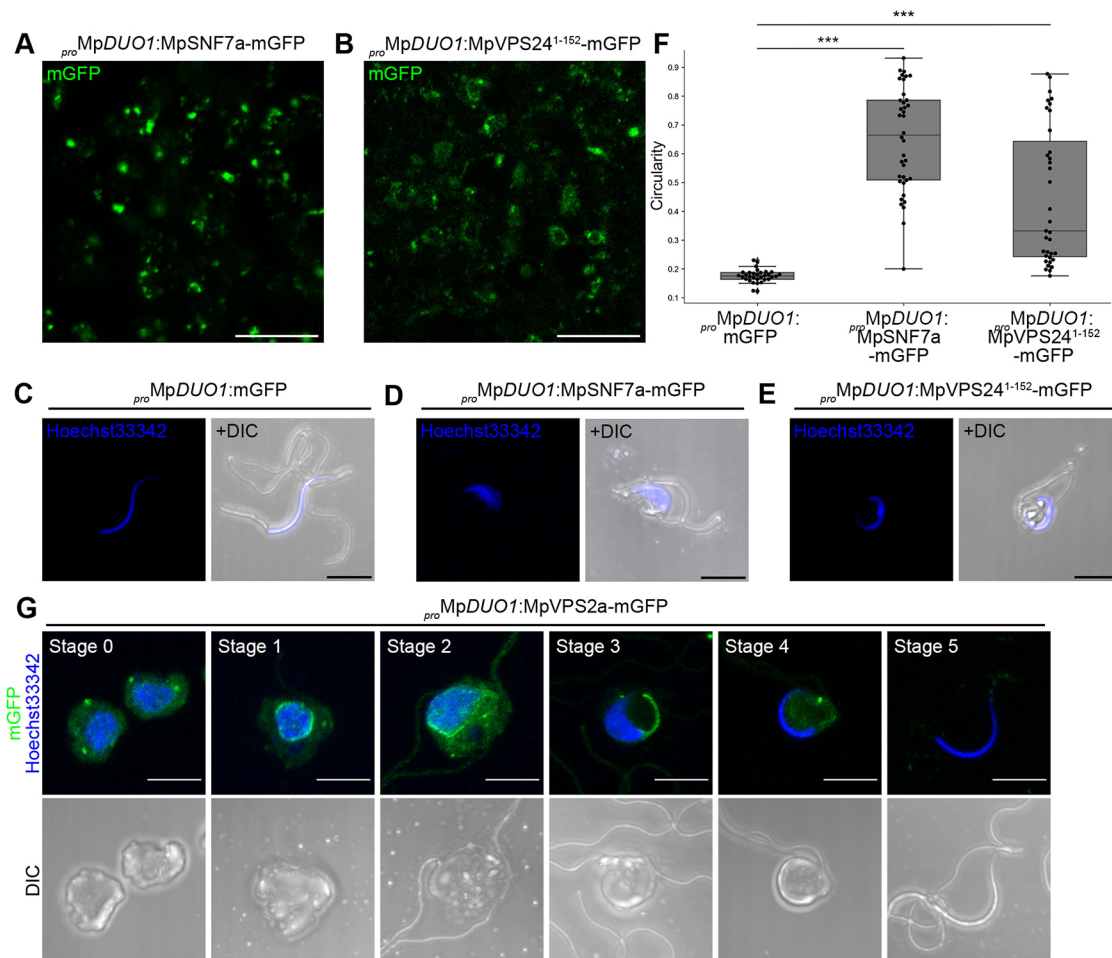


Fig. 7. Dominant-negative perturbation of ESCRT function during spermiogenesis. (A,B) Single confocal images of the spermatogenous tissue expressing MpSNF7a-mGFP (A) or MpVPS24¹⁻¹⁵²-mGFP (B) under the regulation of the *MpDUO1* promoter. Green pseudo-color indicates the fluorescence from mGFP. Scale bars: 10 μ m. Images are representative of 7 (A) and 9 (B) spermatogenous tissues from two independent lines. (C-E) Maximum-intensity projection images of spermatozoa collected from the lines expressing mGFP (C), MpSNF7a-mGFP (D) or MpVPS24¹⁻¹⁵²-mGFP (E) under the regulation of the *MpDUO1* promoter. Left panels show fluorescent images and right panels are merged images with DIC images. Blue pseudo-color indicates the fluorescence from Hoechst 33342. Scale bars: 5 μ m. Images are representative of 25 (C), 27 (D) and 18 (E) cells from two independent lines. (F) Box plots showing the circularity of the nucleus stained with Hoechst 33342. The boxes and solid lines in the boxes indicate the first and third quartiles and the median values, respectively. The upper and lower whiskers are drawn at the greatest value smaller than 1.5 \times interquartile ranges above the third quartile and the smallest value greater than 1.5 \times interquartile ranges below the first quartile, respectively. Asterisks indicate significant differences based on Mann-Whitney's *U*-test ($***P < 0.001$); $n = 32$ for *pro*MpDUO1:mGFP, $n = 38$ for *pro*MpDUO1:MpSNF7a-mGFP and $n = 35$ for *pro*MpDUO1:MpVPS24¹⁻¹⁵²-mGFP. (G) Subcellular localization of MpVPS2a-mGFP driven by the *MpDUO1* promoter in spermatids and a spermatozoid at each developmental stage. Upper panels, fluorescent images; lower panels, DIC images. Green and blue pseudo-colors indicate fluorescence from mGFP and Hoechst 33342, respectively. Scale bars: 5 μ m. Images are representative of 7 (Stage 0), 6 (Stage 1), 6 (Stage 2), 8 (Stage 3), 6 (Stage 4) and 8 (Stage 5) cells.

in the cytosol of spermatids in MpSNF7a-mGFP and MpVPS24¹⁻¹⁵²-mGFP plants at comparable stages (Fig. S6C,D), suggesting that the impairment in ESCRT-III function affects transport to the vacuole and/or protein stability during spermiogenesis.

We also generated transgenic plants expressing an *M. polymorpha* homolog of another ESCRT-III subunit, VPS2, which was C-terminally tagged with mGFP (MpVPS2a-mGFP) (Fig. S6) under the regulation of the *MpDUO1* promoter. *A. thaliana* VPS2 C-terminally tagged with GFP was also reported to act in a dominant-negative manner (Katsiarimpa et al., 2013); however, transgenic plants expressing MpVPS2a-mGFP at moderate levels did not exhibit marked defects in the number and morphology of spermatozoa released into water, distinct from those of the spermatozoa from MpSNF7a-mGFP and MpVPS24¹⁻¹⁵²-mGFP plants (Movie 4). We could therefore

observe the subcellular localization of ESCRT-III during spermiogenesis in these plants. We detected MpVPS2a-mGFP at the punctate structures during stages 0 to 4, which were considered to represent MVEs (Fig. 7G). Intriguingly, MpVPS2a-mGFP was also localized at the periphery of the nucleus during stages 0 to 2 (Fig. 7G). At stage 3, the signal was detected on the string-like structure extending from the posterior side of the nucleus (Fig. 7G). This structure likely represents the 'diverticulum' discovered by TEM analysis, which is an extension of the NE lacking inner chromatin fibrils (Kreitner, 1977b). At stage 4, the signal from MpVPS2a-mGFP was detected only on the punctate structures, which disappeared before stage 5 (Fig. 7G). These results suggest that ESCRT-III, or MpVPS2a by itself, acts at the NE as well as at the MVE during spermiogenesis in *M. polymorpha*.

DISCUSSION

Definition of the developmental stages of spermiogenesis in *M. polymorpha* based on morphological characteristics

A unified criterion for staging developmental processes is useful for developmental studies of any organism, as exemplified by human embryogenesis or spermatogenesis staging, or development of the flower or anther in *A. thaliana* (Bowman et al., 1991; Meistrich and Hess, 2013; O’Rahilly and Müller, 1987; Oakberg, 1956; Sanders et al., 1999). A shared criterion for staging developmental processes would also be useful in studies of plant spermatozoid development. In this study, we propose 1+5 stages of spermiogenesis in *M. polymorpha*, based on the shape of the cell body and the nucleus and formation of the flagella (Fig. 7). The continuous morphological changes of the nucleus in fixed spermatids were roughly classified as spherical, drop-shaped, crescent-shaped or cylinder-shaped (Fig. 1A-F), which is also consistent with previous observations using electron microscopy (Kreitner, 1977b). The change in nuclear morphology during spermiogenesis is accompanied by chromatin condensation, which is associated with the conversion of DNA-binding nuclear basic proteins from histones to protamine-like proteins (D’Ippolito et al., 2019; Higo et al., 2016). Chromatin condensation also occurs during spermiogenesis in animal systems and transcription ceases completely around mid-spermiogenesis as chromatin condensation progresses (Kierszenbaum and Tres, 1975; Sassone-Corsi, 2002). Further progression of spermiogenesis is mediated by the translation of mRNA that is accumulated before spermiogenesis at appropriate time points (Chalmel and Rolland, 2015; Dai et al., 2019). Similar cessation of transcription may occur during spermatogenesis in plants; therefore, morphological characteristics, rather than transcriptome information, would be useful indices for distinguishing the developmental stages of plant spermiogenesis.

Microtubule alternation during spermiogenesis in *M. polymorpha*

After dividing the process of transformation from spermatids to spermatozooids into 1+5 stages, we analyzed microtubule organization in spermatids undergoing spermiogenesis and spermatozooids by immunostaining with antibodies for tubulin or a post-translational modification of tubulin (polyE). At stage 1, microtubules radially extending from the basal region of elongating flagella were observed (Fig. 2B,C). This structure was a transient structure and disappeared before stage 2, at which point flagellar elongation seemed to be nearly complete (Fig. 2D). Therefore, the radial microtubules might function as rails for transporting components of flagella to the bases of the flagella. Similar structures, termed rootlet microtubules, have been observed in *C. reinhardtii*; these extend from the basal bodies and have been involved in arrangement of the eyespot (Boyd et al., 2011). Although spermatids of *M. polymorpha* do not contain the eye spot, the radial structure might be involved in the arrangement of organelles, such as mitochondria, during spermatogenesis. Tubulin of the basal bodies and axonemes undergoes several post-translational modifications, including glutamylation (Janke and Magiera, 2020; Wloga et al., 2017). We found that the flagella and spline in spermatozooids of *M. polymorpha* were recognized by the anti-polyE antibody (Fig. 2; Figs S1, S2), indicating that axonemal and spline microtubules are glutamylated in *M. polymorpha*. Glutamylation is reported to be involved in regulation of flagellar motility in *Chlamydomonas* and *Tetrahymena* (Kubo et al., 2010; Suryavanshi et al., 2010), assembly of doublet microtubules in

mouse (Konno et al., 2016; Lee et al., 2013) and stability of microtubules in *Caenorhabditis elegans* (O’Hagan and Barr, 2012; O’Hagan et al., 2011). The function of the glutamylation of axonemal and spline microtubules in plant spermatozooids should be verified in future studies.

We found that the signals of anti-tubulin antibodies used for immunostaining in this study became weaker as spermiogenesis progressed and then recovered in mature spermatozooids (Fig. 2; Fig. S2). One plausible explanation of this phenomenon is that the state of the post-translational modification of tubulin, including glutamylation, changes as spermiogenesis progresses. The α - and β -tubulin molecules are polyglutamylated at the C-terminal region (Wloga et al., 2017) and epitopes of anti-tubulin antibodies used in this study are also located in the C-terminal region of tubulin molecules. Thus, glutamylation could hinder access of the anti-tubulin antibodies to their epitopes, resulting in diminished signals in immunostaining. This is consistent with the result of immunoblotting; anti- α - and β -tubulin antibodies did not recognize polyglutamylated tubulin, which was detected by the anti-polyE antibody (Fig. S3). Thus, our results indicate that the extent of glutamylation of tubulin molecules may change during spermiogenesis; the degree of glutamylation increases during the formation of the axoneme and, after its completion, microtubules might be deglutamylated. The effects of post-translational modifications of tubulin on microtubule properties in spermatids and spermatozooids and its physiological significance would be interesting topics for further study.

Dynamic reorganization of endomembrane organelles during spermiogenesis

We investigated the reorganization of endomembrane organelles with the progression of spermiogenesis; the results are summarized in Fig. 8, combined with details for the reorganization of mitochondria and plastids from previous studies (Carothers, 1975; Norizuki et al., 2022). The vacuoles changed their morphology and number from complicated and fragmented shapes to a spherical structure at stage 3, when the nucleus assumed a crescent-like shape (Fig. 3C,D). These morphological transitions suggest that vacuoles actively fuse with each other as spermiogenesis proceeds. It would be interesting to see whether evolutionarily conserved machinery components of vacuole biogenesis, such as RAB7/RABG GTPase and the homotypic fusion and protein sorting (HOPS) complex (Brillada et al., 2018; Rojo et al., 2001; Takemoto et al., 2018), are involved in vacuole remodeling during spermiogenesis in *M. polymorpha*, which would also provide useful information for understanding its biological significance. Stage 4 spermatids contained one spherical vacuole in the cell body, whereas the mature spermatozoid had no discernable vacuoles or remnants of the vacuole (Fig. 3E,F). Thus, it appears that the vacuole is removed from the spermatid at the final step of spermiogenesis. In spermiogenesis in *Drosophila melanogaster*, the individualization complex comprising actin cones is required for the elimination of unneeded organelles and the cytosol. The complex is initially formed near the nucleus and moves from the head to the tail of the spermatid. During this movement, the majority of the cytoplasm is removed to form the cystic bulge, which is finally detached from the tip of the tail (Fabian and Brill, 2012). Similarly in plants, actin seems to play an important role in cytoplasm removal during spermiogenesis, although a structure corresponding to the individualization complex in *D. melanogaster* has not been reported (Renzaglia and Garbary, 2001).

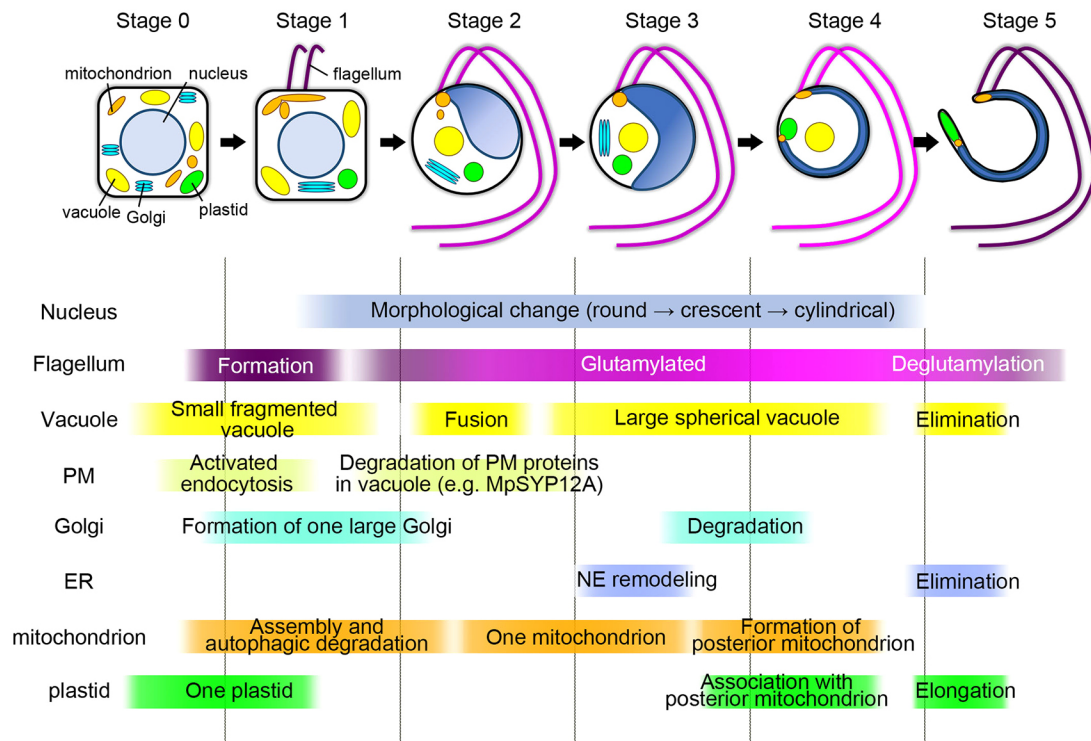


Fig. 8. Schematic diagram of spermiogenesis progression in *M. polymorpha*. Results obtained in this study (remodeling of the nucleus, flagella and endomembrane organelles) are integrated with those of previous studies for remodeling of the mitochondria and plastid (Carothers, 1975; Norizuki et al., 2021 preprint). At stage 0, flagellar formation begins in a cell body and endocytosis is highly activated. One plastid persists through spermiogenesis with dynamic morphological changes. At stage 1, flagella protrude and elongate. Radially extending microtubules are formed from or to the basal region of flagella transiently. Plasma membrane (PM) proteins, including MpSYP12A, are endocytosed and transported to the vacuoles. Mitochondria assemble at the base of the flagella, followed by fission and autophagic degradation. At stage 2, flagellar elongation is mostly complete and morphological change of the nucleus begins. Vacuoles fuse with each other to form a large spherical vacuole. PM proteins are degraded in the spherical vacuoles. One large Golgi apparatus is formed. At stage 3, Golgi proteins are degraded and remodeling of the nuclear envelope occurs. One mitochondrion remains at the base of the flagella. At stage 4, most of the endoplasmic reticulum (ER) proteins are eliminated. A posterior mitochondrion is formed by fission from the anterior mitochondrion and located at the posterior end of the elongated nucleus, associated with the plastid. The spherical vacuole persists until stage 4, which is removed before stage 5 to transform into the mature spermatozoid. The plastid elongates during stages 4 to 5. The glutamylation status of tubulin in the axonemal and spline microtubules alters during spermiogenesis.

Our observation of mCitrine-MpSYP12A revealed that endocytosis of this protein is highly active between stages 0 and 1 (Fig. 4). This result suggests that the protein composition of the PM drastically changes at the early stage of spermiogenesis. The spermatozoid PM must have competence that is distinct from that of the spermatid, such as the ability to respond to an attractant from egg cells and resistance to low osmolarity to prevent rupture in fresh water without the rigid cell wall. Therefore, the cell surface of the spermatozoid is reorganized during spermiogenesis and the high endocytic activity observed in early spermiogenesis might contribute to the thorough remodeling of the PM.

The morphology of the Golgi apparatus has diverged among organisms and even among tissues, probably reflecting diverse and tissue-specific Golgi functions (Ito et al., 2014; Sengupta and Linstedt, 2011). We found that the number and size of the Golgi apparatus changed during spermiogenesis (Fig. 5; Fig. S5), which suggests that the function of the Golgi apparatus changes during spermiogenesis. Furthermore, we found that the signal from Golgi markers disappeared by stage 4, which strongly suggests that the Golgi apparatus (or a major set of Golgi proteins) is eliminated before removal of the cytoplasm. Golgi removal occurs through multiple degradation pathways; Golgi proteins are removed through autophagic and non-autophagic degradation during spermiogenesis in *M. polymorpha* (Minamino et al., 2017; Norizuki et al., 2022).

Drastic deformation of the nucleus during spermiogenesis is generally observed in land plants (Renzaglia and Garbary, 2001). However, the mechanisms of the nuclear remodeling remain unknown. We found that the signal from SP-mCitrine-HDEL and mCitrine-MpSEC22 at the NE was markedly decreased during spermiogenesis, suggesting that the composition of the NE proteins drastically changes during spermiogenesis. Because NE-localized proteins are involved in the regulation of the nuclear shape in *Arabidopsis* (Goswami et al., 2020; Meier et al., 2016), the alteration in composition of the NE might be related to the nuclear reshaping during spermiogenesis in *M. polymorpha*. To our knowledge, the existence of the ER in bryophyte spermatozoids has not been reported (Renzaglia and Garbary, 2001), which suggests that the ER is largely eliminated from spermatozoids. Surprisingly, however, we found that the soluble ER marker remained in the cell body of the spermatozoid (Fig. 6L). It has been reported that the anterior tip of the nucleus is embedded between the spline and anterior mitochondrion during spermiogenesis in *M. polymorpha* (Kreitner, 1977a). The accumulated ER marker at the anterior region of the cell body could represent this anterior tip of the nucleus; soluble luminal ER proteins in this region might escape from degradation. Further analyses would be needed to conclusively demonstrate how the nuclear shaping and ER remodeling are coordinated during spermiogenesis.

The dynamic rearrangement of the NE was further and unexpectedly supported by the observations of MpVPS2a-mGFP. MpVPS2a-mGFP was localized at the periphery of the nucleus, likely at the NE, during the early stages of spermiogenesis. However, this protein was relocated to the extension from the posterior region of the nucleus, which is considered to correspond to the diverticulum. It was hypothesized that the size of the NE is reduced by forming a blebbing structure and/or the diverticulum during spermiogenesis (Kreitner, 1977b). ESCRT-III is involved in NE sealing in animal and yeast cells, which is required during several processes, including the end of open mitosis, NE repair and clearance of nuclear pore complexes (Vietri et al., 2020). Future studies should investigate whether and how ESCRT-III is involved in the dynamic reorganization of the NE during spermiogenesis, which could be required for nuclear shaping given that perturbation of ESCRT-III function caused the formation of an abnormally shaped nucleus (Fig. 7D,E).

Dominant-negative inhibition of ESCRT-III function compromised the motility and shaping of spermatozooids (Fig. 7C-F), which further suggests that the ESCRT-mediated degradation system is required for proper spermiogenesis in *M. polymorpha*. Intriguingly, mCitrine-MpSYP12A signals were not observed in the spherical vacuole or on the vacuolar membrane in spermatids defective in ESCRT function (Fig. S6B-D). In other organisms, the PM proteins accumulate in class E compartment-like structures when ESCRT function is impaired (Teis et al., 2008). One possible explanation for these different effects is that acidification in the aggregates resulted in the abolished mCitrine signal in *M. polymorpha* spermatids. However, it is also possible that a vacuole-independent degradation mechanism compensates for the defective ESCRT-dependent removal of PM proteins. Future studies on the precise molecular functions of ESCRTs during spermiogenesis would unravel how this evolutionarily conserved machinery with multiple functions is recruited to participate in the drastic cellular reorganization processes that have been acquired by plants in a unique manner.

MATERIALS AND METHODS

Plant materials and transformation

Male accession of *Marchantia polymorpha*, Takaragaike-1 (Tak-1), was used throughout this study. Plants were grown on 1/2× Gamborg's B5 medium (FUJIFILM Wako) containing 1.4% (w/v) agar at 22°C under continuous white light. Transformation was performed according to a previously described method (Kubota et al., 2013). Transgenic lines were selected with 10 mg l⁻¹ hygromycin B (FUJIFILM Wako) and 100 mg l⁻¹ cefotaxime (SANOFI) for plants transformed with pMpGWB101-based binary vectors (see below), and 0.5 μM chlorsulfuron (a gift from Dr T. Kohchi, Kyoto University, Japan) and 100 mg l⁻¹ cefotaxime for plants transformed with pMpGWB301-based binary vectors (see below). Induction of sexual organs by far-red irradiation was performed as previously described (Chiyoda et al., 2008).

Constructions

Open reading frames and the sequences of *M. polymorpha* genes were amplified by PCR from cDNA and genomic DNA prepared from Tak-1. Amplified fragments were subcloned into the pENTR/D-TOPO vector (Thermo Fisher Scientific) according to the manufacturer's instructions. The primer sequences and sizes of amplified products are listed in Table S1. To construct pENTR_{pro}MpDUO1 and pENTR_{pro}MpIFT52, the promoter regions of MpDUO1 and MpIFT52 (5.0 and 5.4 kb, respectively) were amplified using Tak-1 genomic DNA, which was subcloned into the pENTR/D-TOPO vector. To construct pENTR_{pro}MpCEN1, the promoter region of MpCEN1 (5.0 kb) was amplified with a SmaI site at the 3' end and subcloned into the pENTR/D-TOPO vector. The resultant sequence was introduced into

pMpGWB307 (a gift from Dr T. Kohchi; Ishizaki et al., 2015) using Gateway LR Clonase II Enzyme Mix (Thermo Fisher Scientific).

To construct pENTR_{pro}MpDUO1:mCitrine, pENTR_{pro}MpCEN1:mCitrine and pENTR_{pro}MpIFT52:mCitrine, MpDUO1, MpCEN1 and MpIFT52 promoter sequences were amplified with a SmaI site at the 3' end and subcloned into the pENTR/D-TOPO vector. The cDNA of mCitrine was amplified and inserted into the SmaI site. To construct pMpGWB101-based and pMpGWB301-based Gateway vectors (Fig. S4D), the promoter regions followed by cDNA for mCitrine or only the promoter regions were amplified from the plasmids described above, which were inserted at the HindIII site of pMpGWB101 or pMpGWB301 using the In-Fusion HD Cloning System (Clontech). To construct pENTR_{pro}MpDUO1:ST-Venus, pENTR_{pro}ST-Venus (Kanazawa et al., 2016; Uemura et al., 2012) was subjected to LR reaction with pMpGWB301_{pro}MpDUO1. To construct pENTR_{pro}MpDUO1:mCitrine-MpSYP12A, pENTR_{pro}MpDUO1:mCitrine-MpVAMP71, pENTR_{pro}MpDUO1:mCitrine-MpGOS11, pENTR_{pro}MpDUO1:mCitrine-MpSFT1 and pENTR_{pro}MpDUO1:mCitrine-MpSEC22, pENTR_{pro}MpSYP12A, pENTR_{pro}MpVAMP71, pENTR_{pro}MpGOS11, pENTR_{pro}MpSFT1 and pENTR_{pro}MpSEC22 (Kanazawa et al., 2016) were subjected to LR recombination with pMpGWB301_{pro}MpDUO1:mCitrine, respectively. To construct pENTR_{pro}MpEF1a:SP-mCitrine-HDEL fusion genes, pDONR_{pro}MpEF1a (Mano et al., 2018) was subjected to LR recombination with R4pMpGWB394 (Mano et al., 2018).

To construct pENTR_{pro}MpDUO1:MpSNF7a-mGFP, pENTR_{pro}MpDUO1:MpVPS24¹⁻¹⁵²-mGFP and pENTR_{pro}MpDUO1:MpVPS2a-mGFP, the coding sequences of MpSNF7a, MpVPS24¹⁻¹⁵² and MpVPS2a were subcloned into the pENTR/D-TOPO vector. cDNA for mGFP was inserted at the AscI site of pENTR_{pro}MpSNF7a, pENTR_{pro}MpVPS24¹⁻¹⁵² and pENTR_{pro}MpVPS2a. The resultant MpSNF7a-mGFP, MpVPS24¹⁻¹⁵²-mGFP and MpVPS2a-mGFP constructs were introduced in pMpGWB101_{pro}MpDUO1 using the In-Fusion HD Cloning System.

Microscopy

To prepare the antheridial cells of *M. polymorpha* for observation, the antheridial receptacles between stages 3 and 5 (Higo et al., 2016) were sliced manually with a razor blade, placed on glass slides (Matsunami) and then covered with coverslips. To prepare the spermatids of *M. polymorpha*, antheridia were fixed for over 60 min with 4% (w/v) paraformaldehyde (PFA) in PME buffer (50 mM PIPES-NaOH, 5 mM EGTA and 1 mM MgSO₄, pH 6.8) and treated for 30 min with cell-wall digestion buffer [1% (w/v) cellulase Onozuka RS (SERVA), 0.25% (w/v) pectolyase Y-23 (Kyowa Chemical Products), 1% (w/v) bovine serum albumin (BSA), 0.1% (v/v) NP-40, 1% (w/v) glucose and 1×Complete EDTA-free protease inhibitor cocktail (Roche Applied Science) in PME buffer]. The samples were placed on glass slides and mounted with PBS containing 0.1% (v/v) Hoechst 33342. To prepare the mature spermatozooids of *M. polymorpha*, collected spermatozooids were fixed for over 60 min with 4% (w/v) PFA in PBS, placed on glass slides, washed with PBS three times and mounted with PBS containing 0.1% (v/v) Hoechst 33342. The prepared samples were observed under LSM780 (Carl Zeiss) with an oil immersion lens (×63). Maximum-intensity projection images and merged images were obtained using Image J (v 1.53q, National Institutes of Health). The circularity, defined as $4\pi S/L^2$ (S, area; L, circumference), of spermatozoid nuclei was calculated using Image J.

For immunostaining spermatids from *M. polymorpha*, we slightly modified the method described in Shimamura (2015). Antheridia were fixed for over 60 min with 4% (w/v) PFA in PME buffer and treated for 30 min with the cell-wall digestion buffer. Cells were then treated with permeabilization buffer [0.01% (v/v) Triton X-100 and 1% (w/v) BSA in PME buffer] for 10 min. After washing with PME buffer three times, cells were placed on adhesive silane-coated glass slides (Matsunami) and incubated for 30 min at room temperature with blocking solution [1% (w/v) BSA in PBS]. After removing the blocking solution, cells were incubated with the primary antibody in PBS at 4°C overnight. After washing with PBS three times, the samples were incubated for 60 min at 37°C with the secondary antibody and 0.1% (v/v) Hoechst 33342 in PBS. After washing with PBS three times, slides were mounted using the ProLong Diamond Antifade reagent (Thermo Fisher Scientific). Immunostaining of mature

spermatozooids was performed almost similar to that of spermatozooids, with an additional centrifugation step at 2000 *g* for 5 min to collect spermatozooids. Samples were observed under LSM780 (Carl Zeiss) with an oil immersion lens ($\times 63$). The reactivities of the antibodies were examined using immunoblotting with cell lysates prepared from the antheridia of Tak-1. Maximum intensity projection images and merged images were obtained by using ImageJ.

For observation of the moving spermatozooids, freshly prepared spermatozooids in distilled water were observed under a dark-field microscope (Olympus) equipped with an ORCA-fusion camera (Hamamatsu Photonics).

Antibodies

The following primary antibodies were used: anti α -tubulin antibody (DM1A, Sigma-Aldrich; 1:1000 for immunostaining), anti α -tubulin antibody (B-5-1-2, Sigma-Aldrich; 1:1000 for immunostaining and immunoblotting), anti β -tubulin antibody (AA2, Abcam; 1:1000 for immunostaining and immunoblotting) and anti polyE antibody (AG25B-0030-C050, AdipoGen Life Sciences; 1:10,000 for immunostaining, 1:5000 for immunoblotting). The secondary antibodies Alexa Fluor 488 Plus goat anti-mouse IgG (A32723; Thermo Fisher Scientific) and Alexa Fluor 594 plus goat anti-rabbit IgG (A32740, Thermo Fisher Scientific) were used at a 1:1000 dilution for immunostaining.

Phylogenetic analysis

Amino acid sequences were collected from the MarpolBase (<https://marchantia.info/>), The Arabidopsis Information Resource (<https://www.arabidopsis.org/>) and the National Center for Biotechnology Information (NCBI) GenBank databases. The gene IDs are listed in Table S2. Collected amino acid sequences were aligned with MAFFT (<https://mafft.cbrc.jp/alignment/server/>; Katoh et al., 2019; Kuraku et al., 2013). After alignment gaps were manually removed, phylogenetic analysis was performed using PhyML 3.0 under the LG model (<http://www.atgc-montpellier.fr/phyml/>; Guindon et al., 2010) with default parameters. Bootstrap analysis was performed by resampling 1000 sets. The obtained tree was processed using FigTree (v1.4.4; <http://tree.bio.ed.ac.uk/software/figtree/>). The multiple alignments used for the phylogenetic analysis are provided in supplementary Materials and Methods (Figs S7 and S8).

Acknowledgements

We thank Dr Takayuki Kohchi (Kyoto University), Dr Ryuichi Nishihama (Tokyo University of Science) and Dr Takehiko Kanazawa (National Institute for Basic Biology, NIBB) for sharing plant materials and plasmids used in this study. We also thank Dr Masaki Shimamura (Hiroshima University) for sharing the protocol for immunostaining. We thank the Model Plant Section, Model Organisms Facility and the NIBB Trans-Scale Biology Center for technical support.

Competing interests

The authors declare no competing or financial interests.

Author contributions

Conceptualization: N.M., T.U.; Investigation: N.M., T.N.; Resources: S.M., K.E.; Writing - original draft: N.M., T.U.; Writing - review & editing: K.E., T.U.; Supervision: T.U.; Funding acquisition: N.M., T.N., K.E., T.U.

Funding

This work was supported by the following grants from the KAKENHI Program of the Japan Society for the Promotion of Science (JSPS): 20K15824 to N.M., 17H05850, 19H04872 and 21K06222 to K.E., and 19H05675, 19H05670 and 21H02515 to T.U., as well as a Grant-in-Aid for JSPS fellows (19J13751 to T.N.).

Peer review history

The peer review history is available online at <https://journals.biologists.com/dev/article-lookup/doi/10.1242/dev.200951>.

References

- Berger, F. and Twell, D. (2011). Germline specification and function in plants. *Annu. Rev. Plant Biol.* **62**, 461-484. doi:10.1146/annurev-arplant-042110-103824
- Bowman, J. L., Drews, G. N. and Meyerowitz, E. M. (1991). Expression of the Arabidopsis floral homeotic gene *AGAMOUS* is restricted to specific cell types late in flower development. *Plant Cell* **3**, 749-758. doi:10.1105/tpc.3.8.749
- Bowman, J. L., Kohchi, T., Yamato, K. T., Jenkins, J., Shu, S., Ishizaki, K., Yamaoka, S., Nishihama, R., Nakamura, Y., Berger, F. et al. (2017). Insights into land plant evolution garnered from the *Marchantia polymorpha* genome. *Cell* **171**, 287-304.e15. doi:10.1016/j.cell.2017.09.030
- Boyd, J. S., Gray, M. M., Thompson, M. D., Horst, C. J. and Dieckmann, C. L. (2011). The daughter four-membered microtubule rootlet determines anterior-posterior positioning of the eyespot in *Chlamydomonas reinhardtii*. *Cytoskeleton* **68**, 459-469. doi:10.1002/cm.20524
- Brazelton, W. J., Amundsen, C. D., Silflow, C. D. and Lefebvre, P. A. (2001). The *bld1* mutation identifies the *Chlamydomonas osm-6* homolog as a gene required for flagellar assembly. *Curr. Biol.* **11**, 1591-1594. doi:10.1016/S0960-9822(01)00485-7
- Brillada, C., Zheng, J., Krüger, F., Rovira-Diaz, E., Askani, J. C., Schumacher, K. and Rojas-Pierce, M. (2018). Phosphoinositides control the localization of HOPS subunit VPS41, which together with VPS33 mediates vacuole fusion in plants. *Proc. Natl. Acad. Sci. USA* **115**, 8305-8314. doi:10.1073/pnas.1807763115
- Cai, Y., Zhuang, X., Gao, C., Wang, X. and Jiang, L. (2014). The Arabidopsis endosomal sorting complex required for transport III regulates internal vesicle formation of the prevacuolar compartment and is required for plant development. *Plant Physiol.* **165**, 1328-1343. doi:10.1104/pp.114.238378
- Carothers, Z. B. (1975). Comparative studies on spermatogenesis in bryophytes. In *The Biology of The Male Gamete*, Vol. 7 (ed. J. G. Duckett and P. A. Racey), pp. 71-84. Biol. J. Linn. Soc. (Supplement No. 1). Academic Press, Inc.
- Carothers, Z. B. and Kreitner, G. L. (1967). Studies of spermatogenesis in the hepaticae. I. Ultrastructure of the *vierergruppe* in *Marchantia*. *J. Cell Biol.* **33**, 43-51. doi:10.1083/jcb.33.1.43
- Carothers, Z. B. and Kreitner, G. L. (1968). Studies of spermatogenesis in the Hepaticae. II. Blepharoplast structure in the spermatid of *Marchantia*. *J. Cell Biol.* **36**, 603-616. doi:10.1083/jcb.36.3.603
- Chalmel, F. and Rolland, A. D. (2015). Linking transcriptomics and proteomics in spermatogenesis. *Reproduction* **150**, 149-157. doi:10.1530/REP-15-0073
- Chiyoda, S., Ishizaki, K., Kataoka, H., Yamato, K. T. and Kohchi, T. (2008). Direct transformation of the liverwort *Marchantia polymorpha* L. by particle bombardment using immature thalli developing from spores. *Plant Cell Rep.* **27**, 1467-1473. doi:10.1007/s00299-008-0570-5
- Dai, P., Wang, X., Gou, L.-T., Li, Z.-T., Wen, Z., Chen, Z.-G., Hua, M.-M., Zhong, A., Wang, L., Su, H. et al. (2019). A translation-activating function of MIWI/piRNA during mouse spermiogenesis. *Cell* **179**, 1566-1581. doi:10.1016/j.cell.2019.11.022
- Deane, J. A., Cole, D. G., Seeley, E. S., Diener, D. R. and Rosenbaum, J. L. (2001). Localization of intraflagellar transport protein IFT52 identifies basal body transitional fibers as the docking site for IFT particles. *Curr. Biol.* **11**, 1586-1590. doi:10.1016/S0960-9822(01)00484-5
- D'Ippolito, R. A., Minamino, N., Rivera-Casas, C., Cheema, M. S., Bai, D. L., Kasinsky, H. E., Shabanowitz, J., Eirin-Lopez, J. M., Ueda, T., Hunt, D. F. et al. (2019). Protamines from liverwort are produced by post-translational cleavage and C-terminal di-aminopropanation of several male germ-specific H1 histones. *J. Biol. Chem.* **294**, 16364-16373. doi:10.1074/jbc.RA119.010316
- Fabian, L. and Brill, J. A. (2012). Drosophila spermiogenesis. *Spermatogenesis* **2**, 197-212. doi:10.4161/spmg.21798
- Gao, C., Luo, M., Zhao, Q., Yang, R., Cui, Y., Zeng, Y., Xia, J. and Jiang, L. (2014). A unique plant ESCRT component, FREE1, regulates multivesicular body protein sorting and plant growth. *Curr. Biol.* **24**, 2556-2563. doi:10.1016/j.cub.2014.09.014
- Goswami, R., Asnacios, A., Hamant, O. and Chabouté, M. E. (2020). Is the plant nucleus a mechanical rheostat? *Curr. Opin. Plant Biol.* **57**, 155-163. doi:10.1016/j.pbi.2020.09.001
- Guindon, S., Dufayard, J.-F., Lefort, V., Anisimova, M., Hordijk, W. and Gascuel, O. (2010). New algorithms and methods to estimate maximum-likelihood phylogenies: assessing the performance of PhyML 3.0. *Sys Biol.* **59**, 307-321. doi:10.1093/sysbio/syq010
- Hackenberg, D. and Twell, D. (2019). The evolution and patterning of male gametophyte development. *Curr. Top. Dev. Biol.* **131**, 257-298. doi:10.1016/bs.ctdb.2018.10.008
- Higo, A., Niwa, M., Yamato, K. T., Yamada, L., Sawada, H., Sakamoto, T., Kurata, T., Shirakawa, M., Endo, M., Shigenobu, S. et al. (2016). Transcriptional framework of male gametogenesis in the liverwort *Marchantia polymorpha* L. *Plant Cell Physiol.* **57**, 325-338. doi:10.1093/pcp/pcw005
- Higo, A., Kawashima, T., Borg, M., Zhao, M., López-Vidriero, I., Sakayama, H., Montgomery, S. A., Sekimoto, H., Hackenberg, D., Shimamura, M. et al. (2018). Transcription factor DUO1 generated by neo-functionalization is associated with evolution of sperm differentiation in plants. *Nat. Commun.* **9**, 1-13. doi:10.1038/s41467-018-07728-3
- Howard, T. L., Stauffer, D. R., Degnin, C. R. and Hollenberg, S. M. (2001). CHMP1 functions as a member of a newly defined family of vesicle trafficking proteins. *J. Cell Sci.* **114**, 2395-2404. doi:10.1242/jcs.114.13.2395
- Ikeno, S. (1903). Beiträge zur Kenntnis der pflanzlichen Spermatogenese: Die Spermatogenese von *Marchantia polymorpha*. *Beihfte zum Botanischen Centralblatt* **15**, 5-88.

- Ishizaki, K., Nishihama, R., Ueda, M., Inoue, K., Ishida, S., Nishimura, Y., Shikanai, T. and Kohchi, T. (2015). Development of gateway binary vector series with four different selection markers for the liverwort *Marchantia polymorpha*. *PLoS One* **10**, 1-13. doi:10.1371/journal.pone.0138876
- Isono, E. (2021). ESCRT is a great sealer: Non-endosomal function of the ESCRT machinery in membrane repair and autophagy. *Plant Cell Physiol.* **62**, 766-774. doi:10.1093/pcp/pcab045
- Isono, E., Katsiarimpa, A., Müller, I. K., Anzenberger, F., Stierhof, Y.-D., Geldner, N., Chory, J. and Schwechheimer, C. (2010). The deubiquitinating enzyme AMSH3 is required for intracellular trafficking and vacuole biogenesis in *Arabidopsis thaliana*. *Plant Cell* **22**, 1826-1837. doi:10.1105/tpc.110.075952
- Ito, Y., Uemura, T. and Nakano, A. (2014). Formation and maintenance of the Golgi apparatus in plant cells. *Int. Rev. Cell Mol. Biol.* **310**, 221-287. doi:10.1016/B978-0-12-800180-6.00006-2
- Janke, C. and Magiera, M. M. (2020). The tubulin code and its role in controlling microtubule properties and functions. *Nat. Rev. Mol. Cell Biol.* **21**, 307-326. doi:10.1038/s41580-020-0214-3
- Kanazawa, T., Era, A., Minamino, N., Shikano, Y., Fujimoto, M., Uemura, T., Nishihama, R., Yamato, K. T., Ishizaki, K., Nishiyama, T. et al. (2016). SNARE molecules in *Marchantia polymorpha*: Unique and conserved features of the membrane fusion machinery. *Plant Cell Physiol.* **57**, 307-324. doi:10.1093/pcp/pcv076
- Katoh, K., Rozewicki, J. and Yamada, K. D. (2019). MAFFT online service: multiple sequence alignment, interactive sequence choice and visualization. *Brief. Bioinform.* **20**, 1160-1166. doi:10.1093/bib/bbx108
- Katsiarimpa, A., Anzenberger, F., Schlager, N., Neubert, S., Hauser, M.-T., Schwechheimer, C. and Isono, E. (2011). The *Arabidopsis* deubiquitinating enzyme AMSH3 interacts with ESCRT-III subunits and regulates their localization. *Plant Cell* **23**, 3026-3040. doi:10.1105/tpc.111.087254
- Katsiarimpa, A., Kalinowska, K., Anzenberger, F., Weis, C., Ostertag, M., Tsutsumi, C., Schwechheimer, C., Brunner, F., Hückelhoven, R. and Isono, E. (2013). The deubiquitinating enzyme AMSH1 and the ESCRT-III subunit VPS2.1 are required for autophagic degradation in *Arabidopsis*. *Plant Cell* **25**, 2236-2252. doi:10.1105/tpc.113.113399
- Kierszenbaum, A. L. and Tres, L. L. (1975). Structural and transcriptional features of the mouse spermatid genome. *J. Cell Biol.* **65**, 258-270. doi:10.1083/jcb.65.2.258
- Klink, V. P. and Wolniak, S. M. (2001). Centrin is necessary for the formation of the motile apparatus in spermatids of *Marsilea*. *Mol. Biol. Cell.* **12**, 761-776. doi:10.1091/mbc.12.3.761
- Kohchi, T., Yamato, K. T., Ishizaki, K., Yamaoka, S. and Nishihama, R. (2021). Development and molecular genetics of *Marchantia polymorpha*. *Annu. Rev. Plant Biol.* **72**, 19-20. doi:10.1146/annurev-arplant-082520-094256
- Koi, S., Hisanaga, T., Sato, K., Shimamura, M., Yamato, K. T., Ishizaki, K., Kohchi, T. and Nakajima, K. (2016). An evolutionarily conserved plant RKD factor controls germ cell differentiation. *Curr. Biol.* **26**, 1775-1781. doi:10.1016/j.cub.2016.05.013
- Kolb, C., Nagel, M.-K., Kalinowska, K., Hagmann, J., Ichikawa, M., Anzenberger, F., Alkofer, A., Sato, M. H., Braun, P. and Isono, E. (2015). FYVE1 is essential for vacuole biogenesis and intracellular trafficking in *Arabidopsis*. *Plant Physiol.* **167**, 1361-1373. doi:10.1104/pp.114.253377
- Konno, A., Ikegami, K., Konishi, Y., Yang, H. J., Abe, M., Yamazaki, M., Sakimura, K., Yao, I., Shiba, K., Inaba, K. et al. (2016). *Tll9*^{-/-} mice sperm flagella show shortening of doublet 7, reduction of doublet 5 polyglutamylation and a stall in beating. *J. Cell Sci.* **129**, 2757-2766. doi:10.1242/jcs.185983
- Koshimizu, S., Kofuji, R., Sasaki-Sekimoto, Y., Kikkawa, M., Shimajima, M., Ohta, H., Shigenobu, S., Kabeya, Y., Hiwatashi, Y., Tamada, Y. et al. (2018). *Physcomitrella* MADS-box genes regulate water supply and sperm movement for fertilization. *Nat. Plants* **4**, 36-45. doi:10.1038/s41477-017-0082-9
- Kreitner, G. L. (1977a). Influence of the multilayered structure on the morphogenesis of *Marchantia* spermatids. *Am. J. Bot.* **64**, 57-64. doi:10.1002/j.1537-2197.1977.tb07605.x
- Kreitner, G. L. (1977b). Transformation of the nucleus in *Marchantia* spermatids: morphogenesis. *Am. J. Bot.* **64**, 464-475. doi:10.1002/j.1537-2197.1977.tb12370.x
- Kreitner, G. L. and Carothers, Z. B. (1976). Studies of spermatogenesis in the Hepaticae V. Blepharoplast development in *Marchantia polymorpha*. *Am. J. Bot.* **63**, 545-557. doi:10.1002/j.1537-2197.1976.tb11843.x
- Kubo, T., Yanagisawa, H.-A., Yagi, T., Hirono, M. and Kamiya, R. (2010). Tubulin polyglutamylation regulates axonemal motility by modulating activities of inner-arm dyneins. *Curr. Biol.* **20**, 441-445. doi:10.1016/j.cub.2009.12.058
- Kubo, T., Yanagisawa, H.-A., Liu, Z., Shibuya, R., Hirono, M. and Kamiya, R. (2014). A conserved flagella-associated protein in *Chlamydomonas*, FAP234, is essential for axonemal localization of tubulin polyglutamylation TLL9. *Mol. Biol. Cell* **25**, 107-117. doi:10.1091/mbc.e13-07-0424
- Kubota, A., Ishizaki, K., Hosaka, M. and Kohchi, T. (2013). Efficient agrobacterium-mediated transformation of the liverwort *Marchantia polymorpha* using regenerating thalli. *Biosci. Biotechnol. Biochem.* **77**, 167-172. doi:10.1271/bbb.120700
- Kuraku, S., Zmasek, C. M., Nishimura, O. and Katoh, K. (2013). aLeaves facilitates on-demand exploration of metazoan gene family trees on MAFFT sequence alignment server with enhanced interactivity. *Nucleic Acids Res.* **41**, W22-W28. doi:10.1093/nar/gkt389
- Lee, G.-S., He, Y., Dougherty, E. J., Jimenez-Movilla, M., Avella, M., Grullon, S., Shalin, D. S., Guo, C., Blackford, J. A., Jr, Awasthi, S. et al. (2013). Disruption of *Tll5/Stamp* gene (tubulin tyrosine ligase-like protein 5/SRC-1 and TIF2-associated modulatory protein gene) in male mice causes sperm malformation and infertility. *J. Biol. Chem.* **288**, 15167-15180. doi:10.1074/jbc.M113.453936
- Mano, S., Nishihama, R., Ishida, S., Hikino, K., Kondo, M., Nishimura, M., Yamato, K. T., Kohchi, T. and Nakagawa, T. (2018). Novel gateway binary vectors for rapid tripartite DNA assembly and promoter analysis with various reporters and tags in the liverwort *Marchantia polymorpha*. *PLoS One* **13**, e0204964. doi:10.1371/journal.pone.0204964
- Meier, I., Griffis, A. H. N., Groves, N. R. and Wagner, A. (2016). Regulation of nuclear shape and size in plants. *Curr. Opin. Cell Biol.* **40**, 114-123. doi:10.1016/j.cub.2016.03.005
- Meistrich, M. L. and Hess, R. A. (2013). Assessment of spermatogenesis through staging of seminiferous tubules. *Methods Mol. Biol.* **927**, 299-307. doi:10.1007/978-1-62703-038-0_27
- Minamino, N., Kanazawa, T., Nishihama, R., Yamato, K. T., Ishizaki, K., Kohchi, T., Nakano, A. and Ueda, T. (2017). Dynamic reorganization of the endomembrane system during spermatogenesis in *Marchantia polymorpha*. *J. Plant Res.* **130**, 433-441. doi:10.1007/s10265-017-0909-5
- Minamino, N., Kanazawa, T., Era, A., Ebine, K., Nakano, A. and Ueda, T. (2018). RAB GTPases in the basal land plant *Marchantia polymorpha*. *Plant Cell Physiol.* **59**, 845-856. doi:10.1093/pcp/pcy027
- Montgomery, S. A., Tanizawa, Y., Galik, B., Wang, N., Ito, T., Mochizuki, T., Akimcheva, S., Bowman, J. L., Cognat, V., Maréchal-Drouard, L. et al. (2020). Chromatin organization in early land plants reveals an ancestral association between H3K27me3, transposons, and constitutive heterochromatin. *Curr. Biol.* **30**, 573-588.e7. doi:10.1016/j.cub.2019.12.015
- Nagel, M. K., Kalinowska, K., Vogel, K., Reynolds, G. D., Wu, Z., Anzenberger, F., Ichikawa, M., Tsutsumi, C., Sato, M. H., Kuster, B. et al. (2017). *Arabidopsis* SH3P2 is an ubiquitin-binding protein that functions together with ESCRT-I and the deubiquitylating enzyme AMSH3. *Proc. Natl. Acad. Sci. USA* **114**, 7197-7204. doi:10.1073/pnas.1710866114
- Norizuki, T., Minamino, N., Sato, M., Tsukaya, H. and Ueda, T. (2022). Dynamic rearrangement and autophagic degradation of mitochondria during spermiogenesis in the liverwort *Marchantia polymorpha*. *Cell Rep.* **39**, 110975. doi:10.1016/j.celrep.2022.110975
- Oakberg, E. F. (1956). A description of spermiogenesis in the mouse and its use in analysis of the cycle of the seminiferous epithelium and germ cell renewal. *Am. J. Anat.* **99**, 391-413. doi:10.1002/aja.1000990303
- O'Hagan, R. and Barr, M. M. (2012). Regulation of tubulin glutamylation plays cell-specific roles in the function and stability of sensory cilia. *Worm* **1**, 155-159. doi:10.4161/worm.19539
- O'Hagan, R., Piasecki, B. P., Silva, M., Phirke, P., Nguyen, K. C. Q., Hall, D. H., Swoboda, P. and Barr, M. M. (2011). The tubulin deglutamylase CAPP-1 regulates the function and stability of sensory cilia in *C. elegans*. *Curr. Biol.* **21**, 1685-1694. doi:10.1016/j.cub.2011.08.049
- O'Rahilly, R. and Müller, F. (1987). *Developmental Stages in Human Embryos, Including a Revision of Streeter's 'Horizons' and a Survey of the Carnegie Collection*. Washington: Carnegie Institution of Washington.
- Raymond, C. K., Howald-Stevenson, I., Vater, C. A. and Stevens, T. H. (1992). Morphological classification of the yeast vacuolar protein sorting mutants: evidence for a prevacuolar compartment in class E vps mutants. *Mol. Biol. Cell* **3**, 1389-1402. doi:10.1091/mbc.3.12.1389
- Renzaglia, K. S. and Duckett, J. G. (1987). Spermatogenesis in *Blasia pusilla*: from young antheridium through mature spermatozoid. *Bryologist* **90**, 419. doi:10.2307/3243109
- Renzaglia, K. S. and Garbary, D. J. (2001). Motile gametes of land plants: diversity, development, and evolution. *CRC. Crit. Rev. Plant Sci.* **20**, 107-213. doi:10.1080/20013591099209
- Reider, S. E., Banta, L. M., Köhrer, K., McCaffery, J. M. and Emr, S. D. (1996). Multilamellar endosome-like compartment accumulates in the yeast vps28 vacuolar protein sorting mutant. *Mol. Biol. Cell* **7**, 985-999. doi:10.1091/mbc.7.6.985
- Rojo, E., Gillmor, C. S., Kovaleva, V., Somerville, C. R. and Raikhel, N. V. (2001). *VACUOLELESS1* is an essential gene required for vacuole formation and morphogenesis in *Arabidopsis*. *Dev. Cell* **1**, 303-310. doi:10.1016/S1534-5807(01)00024-7
- Russell, S. D. and Jones, D. S. (2015). The male germline of angiosperms: repertoire of an inconspicuous but important cell lineage. *Front. Plant Sci.* **6**, 1-10. doi:10.3389/fpls.2015.00173
- Sanchez-Vera, V., Kenchappa, C. S., Landberg, K., Bressendorff, S., Schwarzbach, S., Martin, T., Mundy, J., Petersen, M., Thelander, M. and Sundberg, E. (2017). Autophagy is required for gamete differentiation in the moss *Physcomitrella patens*. *Autophagy* **13**, 1939-1951. doi:10.1080/15548627.2017.1366406

- Sanders, P. M., Bui, A. Q., Weterings, K., McIntire, K. N., Hsu, Y.-C., Lee, P. Y., Truong, M. T., Beals, T. P. and Goldberg, R. B.** (1999). Anther developmental defects in *Arabidopsis thaliana* male-sterile mutants. *Sex. Plant Reprod.* **11**, 297-322. doi:10.1007/s004970050158
- Sassone-Corsi, P.** (2002). Unique chromatin remodeling and transcriptional regulation in spermatogenesis. *Science* **296**, 2176-2178. doi:10.1126/science.1070963
- Sengupta, D. and Linstedt, A. D.** (2011). Control of organelle size: the Golgi complex. *Annu. Rev. Cell Dev. Biol.* **27**, 57-77. doi:10.1146/annurev-cellbio-100109-104003
- Shimamura, M.** (2015). Whole-mount immunofluorescence staining of plant cells and tissues. In *Plant Microtechniques and Protocols* (ed. E. Yeung), pp. 181-196. Switzerland: Springer.
- Shimamura, M.** (2016). *Marchantia polymorpha*: taxonomy, phylogeny and morphology of a model system. *Plant Cell Physiol.* **57**, 230-256. doi:10.1093/pcp/pcv192
- Spitzer, C., Reyes, F. C., Buono, R., Sliwinski, M. K., Haas, T. J. and Otegui, M. S.** (2009). The ESCRT-related CHMP1A and B proteins mediate multivesicular body sorting of auxin carriers in *Arabidopsis* and are required for plant development. *Plant Cell* **21**, 749-766. doi:10.1105/tpc.108.064865
- Suryavanshi, S., Eddé, B., Fox, L. A., Guerrero, S., Hard, R., Hennessey, T., Kabi, A., Malison, D., Pennock, D., Sale, W. S. et al.** (2010). Tubulin glutamylation regulates ciliary motility by altering inner dynein arm activity. *Curr. Biol.* **20**, 435-440. doi:10.1016/j.cub.2009.12.062
- Takemoto, K., Ebine, K., Askani, J. C., Krüger, F., Gonzalez, Z. A., Ito, E., Goh, T., Schumacher, K., Nakano, A. and Ueda, T.** (2018). Distinct sets of tethering complexes, SNARE complexes, and Rab GTPases mediate membrane fusion at the vacuole in *Arabidopsis*. *Proc. Natl. Acad. Sci. USA* **115**, 2457-2466. doi:10.1073/pnas.1717839115
- Teis, D., Saksena, S. and Emr, S. D.** (2008). Ordered assembly of the ESCRT-III complex on endosomes is required to sequester cargo during MVB formation. *Dev. Cell.* **15**, 578-589. doi:10.1016/j.devcel.2008.08.013
- Teis, D., Saksena, S., Judson, B. L. and Emr, S. D.** (2010). ESCRT-II coordinates the assembly of ESCRT-III filaments for cargo sorting and multivesicular body vesicle formation. *EMBO J.* **29**, 871-883. doi:10.1038/emboj.2009.408
- Twell, D.** (2011). Male gametogenesis and germline specification in flowering plants. *Sex. Plant Reprod.* **24**, 149-160. doi:10.1007/s00497-010-0157-5
- Uemura, T., Kim, H., Saito, C., Ebine, K., Ueda, T., Schulze-Lefert, P. and Nakano, A.** (2012). Qa-SNAREs localized to the *trans*-Golgi network regulate multiple transport pathways and extracellular disease resistance in plants. *Proc. Natl. Acad. Sci. USA* **109**, 1784-1789. doi:10.1073/pnas.1115146109
- Vietri, M., Radulovic, M. and Stenmark, H.** (2020). The many functions of ESCRTs. *Nat. Rev. Mol. Cell Biol.* **21**, 25-42. doi:10.1038/s41580-019-0177-4
- Vu, H. T., Akatsu, H., Hashizume, Y., Setou, M. and Ikegami, K.** (2016). Increase in α -tubulin modifications in the neuronal processes of hippocampal neurons in both kainic acid-induced epileptic seizure and Alzheimer's disease. *Sci. Rep.* **7**, 40205. doi:10.1038/srep40205
- Wloga, D., Joachimiak, E., Louka, P. and Gaertig, J.** (2017). Posttranslational modifications of Tubulin and cilia. *Cold Spring Harb. Perspect. Biol.* **9**, a028159. doi:10.1101/cshperspect.a028159
- Zhang, X.-Q., Hou, P., Zhu, H.-T., Li, G.-D., Liu, X.-G. and Xie, X.-M.** (2013). Knockout of the VPS22 component of the ESCRT-II complex in rice (*Oryza sativa* L.) causes chalky endosperm and early seedling lethality. *Mol. Biol. Rep.* **40**, 3475-3481. doi:10.1007/s11033-012-2422-1

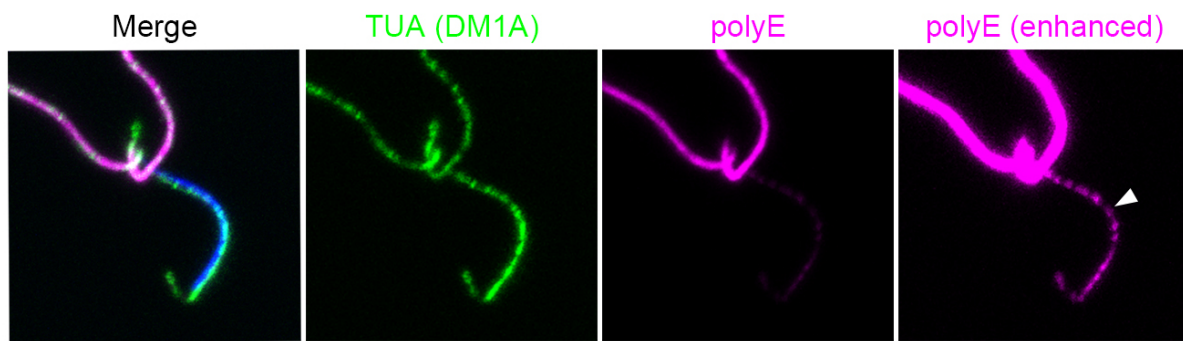


Fig. S1. Immunostaining of spermatozoids with anti- α -tubulin and anti-polyE antibodies

(A) Maximum intensity projection images of a spermatozoid immunostained with anti-polyE and anti- α -tubulin (TUA (DM1A)) antibodies. An arrowhead indicates the signal of polyE along the spline. The image is representative of 11 cells.

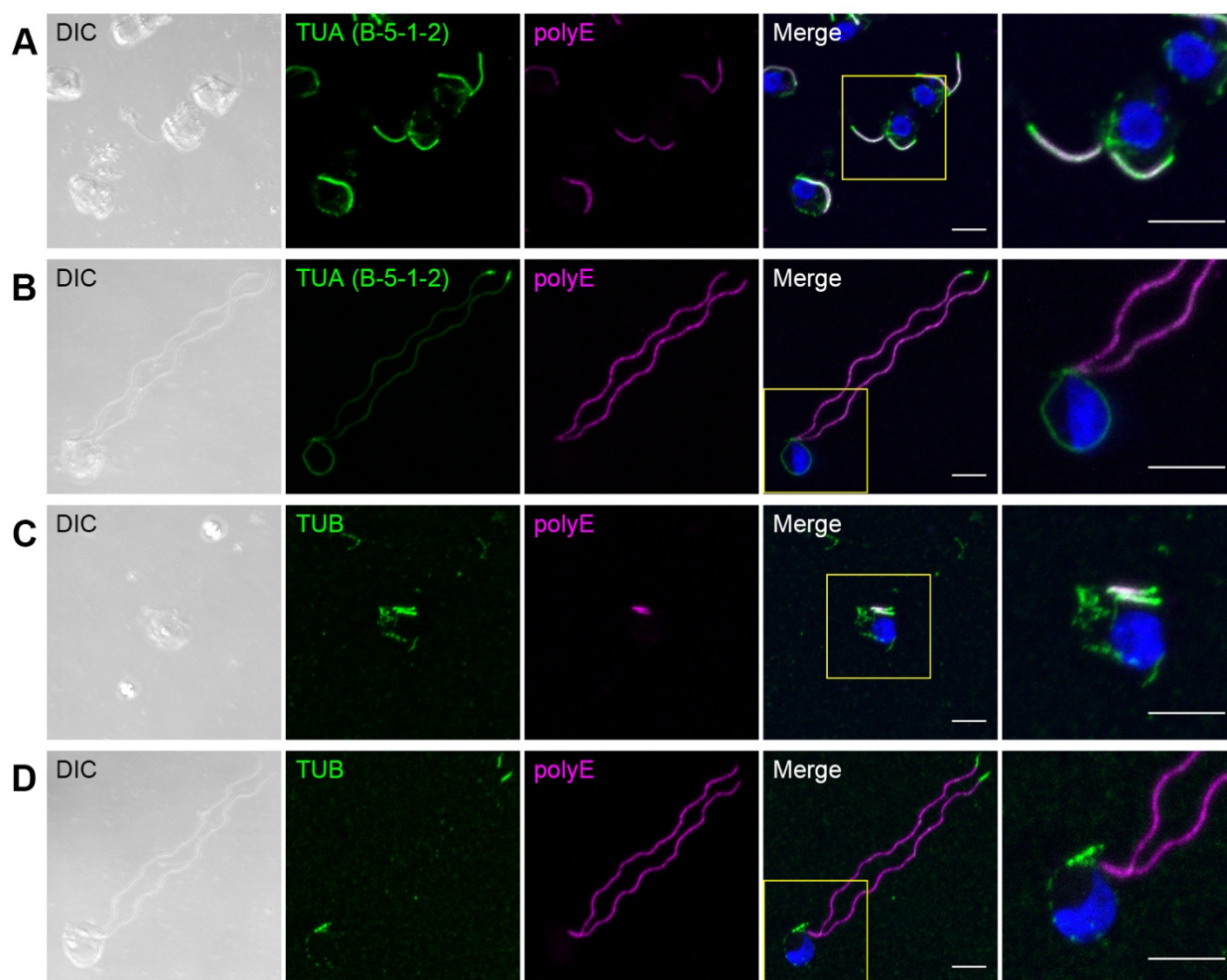


Fig. S2. Immunostaining of spermatids with distinct anti-tubulin antibodies

(A–D) Maximum intensity projection images of spermatids immunostained with anti-polyE and anti- α -tubulin (A and B) or β -tubulin (C and D) antibodies. The leftmost panels, differential interference contrast (DIC) images; other panels, fluorescence images. The rightmost panels are high magnification images of yellow-squared areas. Green, magenta, and blue pseudo-colors indicate fluorescence of Alexa 488 (α -tubulin or β -tubulin), Alexa 594 (polyE), and Hoechst 33342, respectively. Scale bars = 5 μ m. Images are representative of 8 (A), 6 (B), 5 (C), and (9) cells.

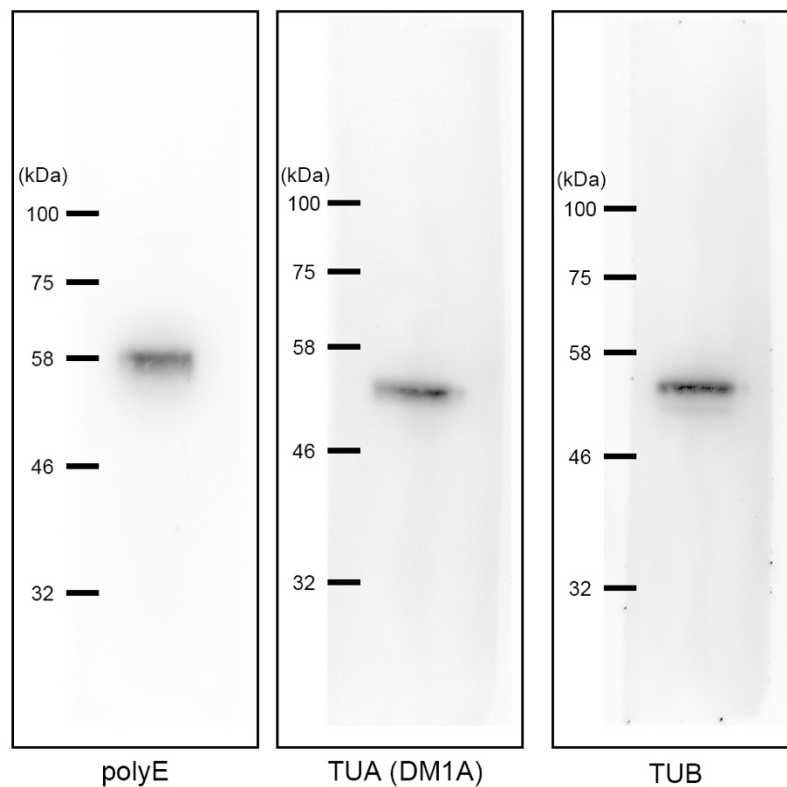


Fig. S3. Anti-tubulin and anti-polyE antibodies react with distinct populations of tubulin.

Immunoblotting using cell lysates prepared from antheridia of Tak-1 with anti- α -tubulin (TUA (DM1A)), anti- β -tubulin (TUB (AA2)), and anti-polyE antibodies. Black bars indicate molecular weights (kDa). Immunoblotting was repeated three times for each antibody.

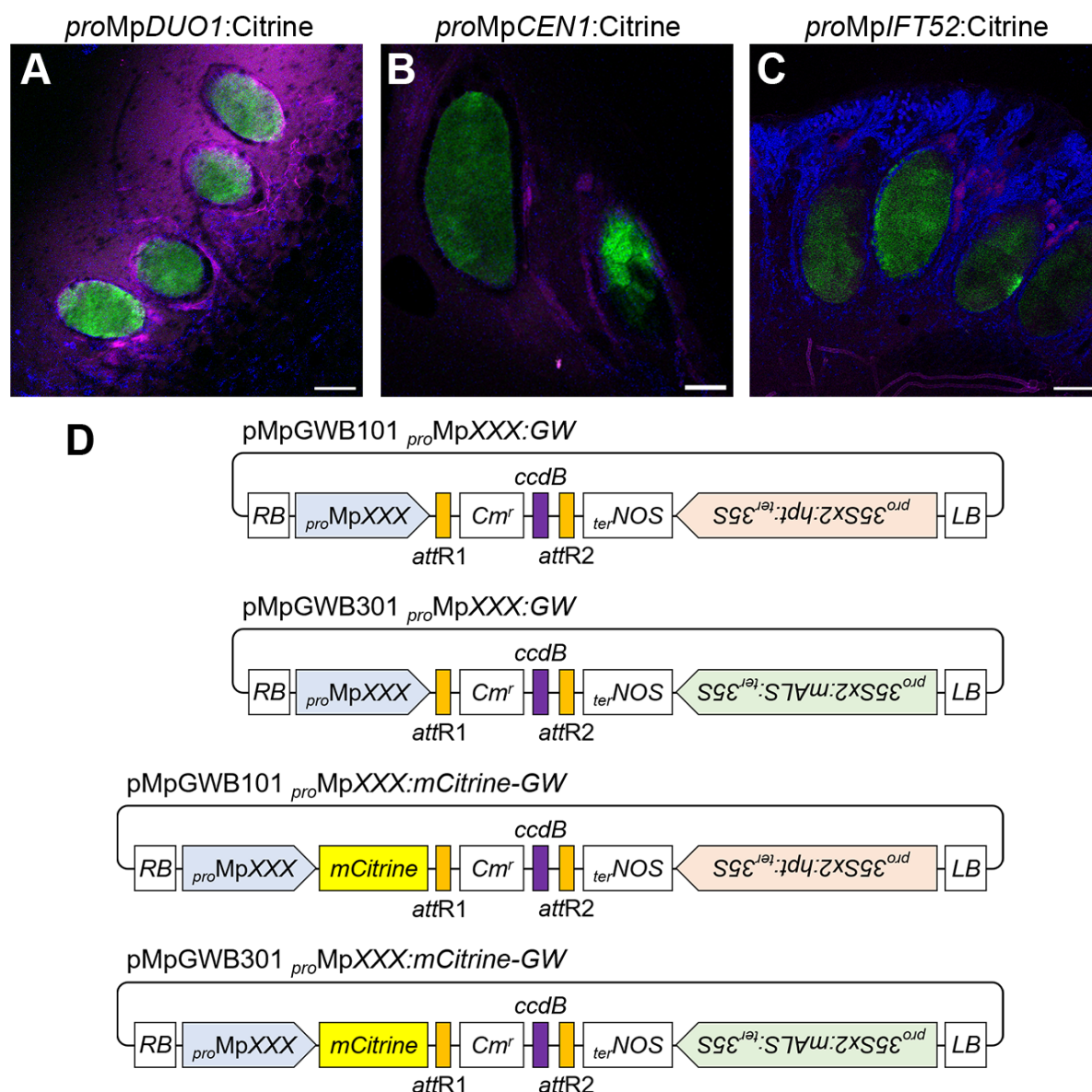


Fig. S4. Spermatid-dominant expression by promoters of *MpDUO1*, *MpCEN1*, and *MpIFT52*

(A–C) Maximum intensity projection images of sliced antheridial receptacles transformed with *proMpDUO1:Citrine* (A), *proMpCEN1:Citrine* (B), or *proMpIFT52:Citrine* (C). Green, red, and blue pseudo-colors indicate fluorescence from Citrine, anthocyanin-like compound, and chlorophyll, respectively. Scale bars = 10 μ m. Images are representative of 3 (A), 3 (B), and 4 (C) receptacles. (D) Schematic illustration of Gateway vectors.

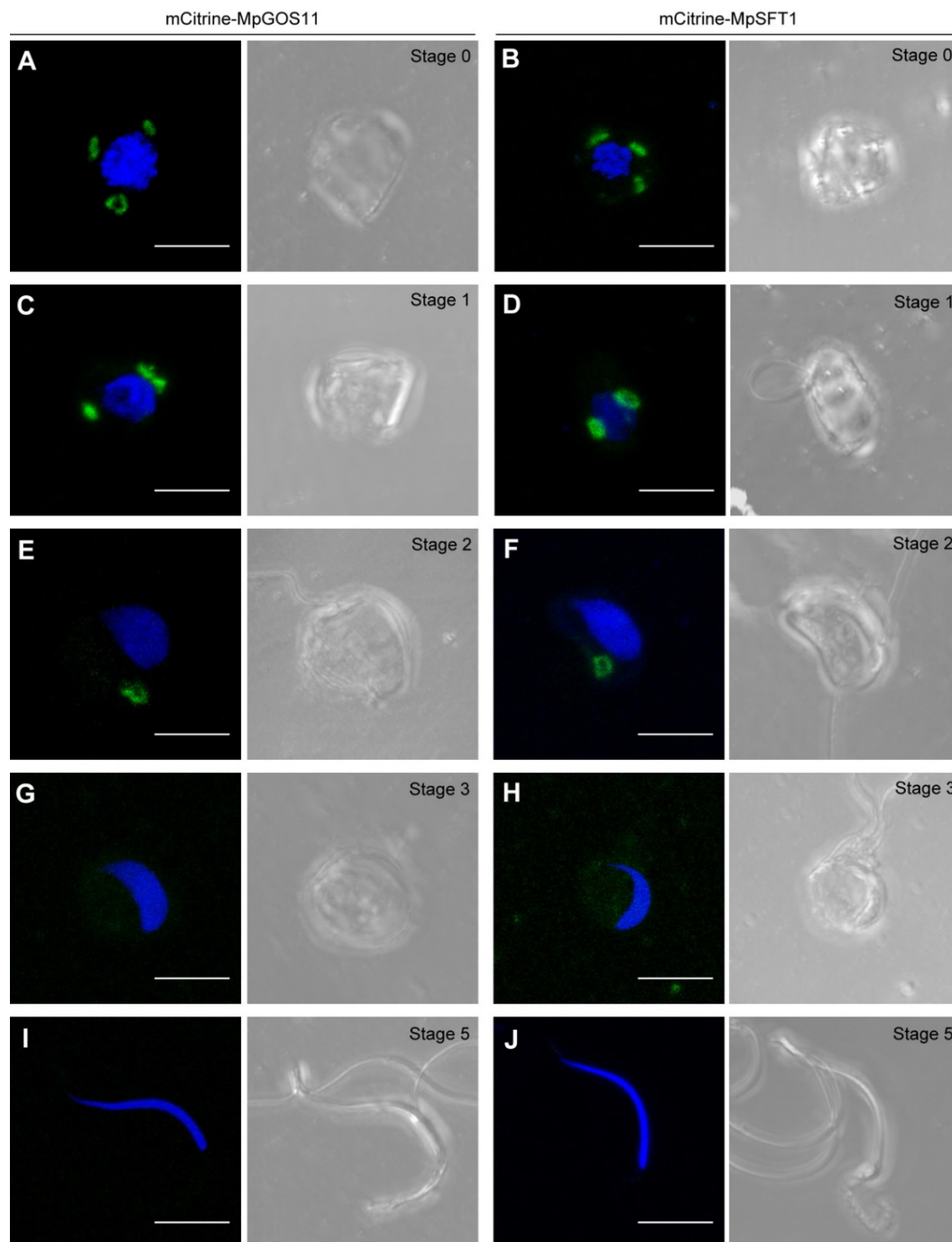


Fig. S5. Reorganization of the Golgi apparatus during spermiogenesis

Maximum intensity projection images of spermatids and spermatozooids expressing mCitrine-MpGOS11 (A, C, E, G, I) or mCitrine-MpSFT1 (B, D, F, H, J) driven by the *MpDUO1* promoter. Left panels, fluorescence images; right panels, differential interference contrast (DIC) images. Green and blue pseudo colors indicate fluorescence from mCitrine and Hoechst 33342, respectively. Scale bars = 5 μ m. Each image is representative of at least 30 cells from four (mCitrine-MpGOS11) or six (mCitrine-MpSFT1) independent lines.

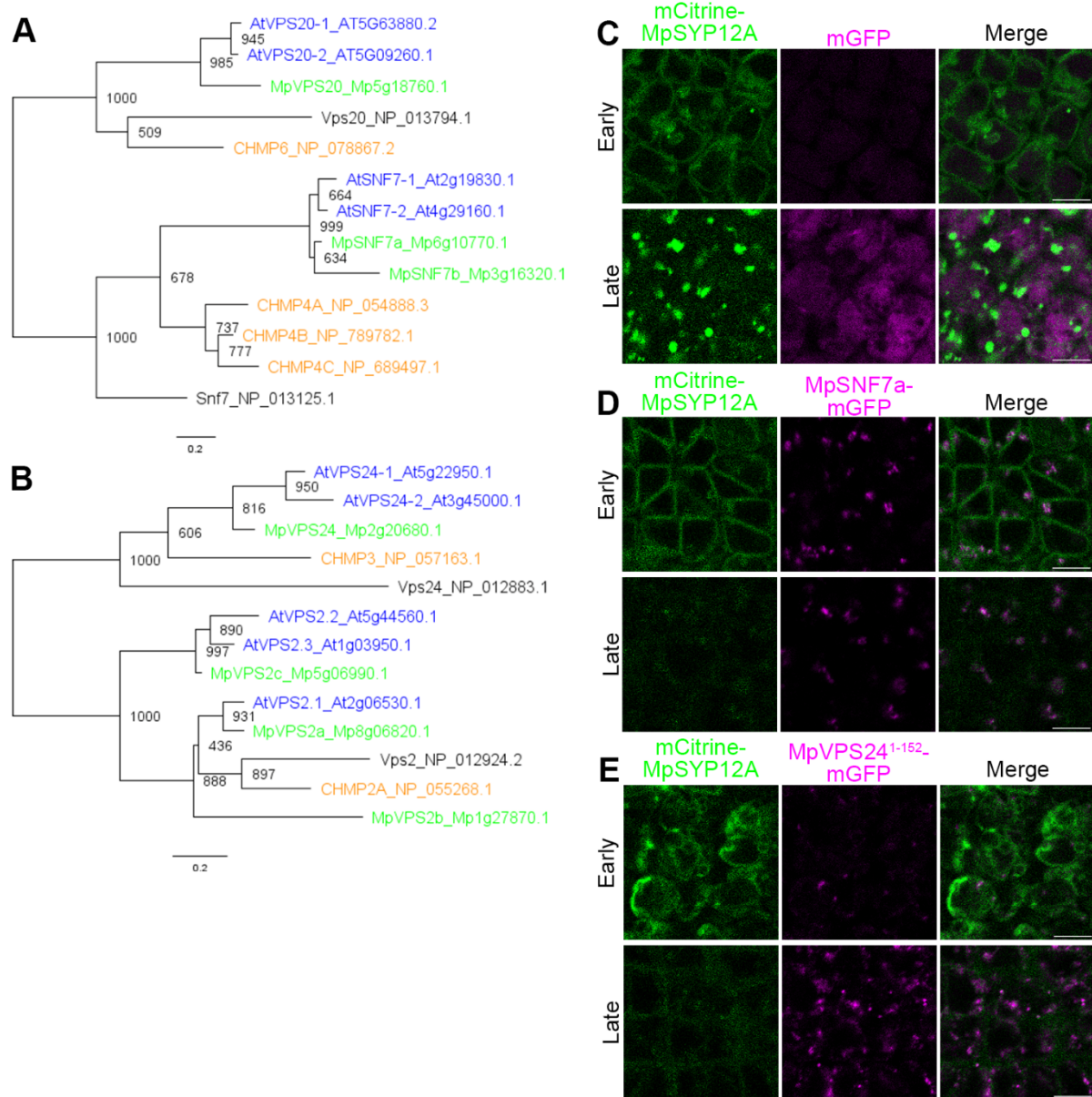


Fig. S6. Phylogenetic analysis of MpESCRT-III proteins and effects of dominant-negative ESCRTs on the reorganization of plasma membrane proteins in spermatids.

(A–B) Maximum-likelihood phylogenetic trees for the Snf7-domain family (VPS20 and SNF7) and the Vps24-domain family (VPS24 and VPS2) of ESCRT-III subunits (Leung et al., 2008). Protein sequences were collected from genome databases of *Arabidopsis thaliana* (blue), *Marchantia polymorpha* (lime green), *Homo sapiens* (dark orange), and *Saccharomyces cerevisiae* (black). The bootstrap probabilities are indicated on each branch. The alignment of protein sequences used for construction of the tree is shown in Figs S7 and S8. (C–E) Single confocal images of spermatids expressing mCitrine-MpSYP12A driven by its own promoter and mGFP (C), MpSNF7a-mGFP (D), or MpVPS24¹⁻¹⁵²-mGFP (E) driven by the MpDUO1 promoter. Green and magenta pseudo-colors indicate fluorescence from mCitrine and mGFP, respectively. Scale bars = 5 μ m. Images are representative of 2 (C, Early), 5 (C, Late), 2 (D, Early), 8 (D, Late), 4 (E, Early), and 6 (E, Late) tissues from independent two lines.

MpSNF7A_Mp6g10770.1	TLDKLNETLEMLEKKEKVLQKKIAVEIEKARDYTRKNKRAAIQCLKKKKLYEVQVEQLGN
AtSNF7-2_At4g29160.1	TLDKLNETLEMLEKKEKVLKKAGAEVEKAKEYSRKNKRAAIQCLKRKRLYEGQVEQLGN
AtSNF7-1_At2g19830.1	--LLLVQTLEMLEKKENVLLKKATGEVEKAKEFSRKNKRAAIQCLKRKRLYEQQVEQLGN
MpSNF7B_Mp3g16320.1	SMEKIGENLDMLEKKEQILQRKIAAELQKATEYSKKNKRAAINCLKKKKLFEAQAEQLAA
CHMP4A_NP_054888.3	AIQKLKETEKILIKKQEFLEQKIQQELQTAKKYGTKNKRAALQALRRKKRFEQQLAQTDG
CHMP4B_NP_789782.1	AIQRLRDTEEMLSKKQEFLEKKIEQELTAAKKHGTKNKRAALQALRRKKRYEKQLAQIDG
CHMP4C_NP_689497.1	ALVRLRETEEMLGKKQEYLENRIQREIALAKKHGTQNKRAALQALRRKKRFEKQLTQIDG
Snf7_NP_013125.1	AIVRLREHINLLSKKQSHLRTQITNQENEARIFLTGNKVMKNALKKKKKTIEQLLSKVEG
AtVPS20-1_AT5G63880.2	AILSLKTQRRKLGQYQQKLEKIVIEAEKQAARDLIRKRKDRALLALRRKRTQEELLKQVDQ
AtVPS20-2_AT5G09260.1	AILSLKTQRRKLGQYQQKLEKIVIEAEKQAARDLIRKRKDRALLALRRKRTQEELLKQVDQ
MpVPS20_Mp5g18760.1	AILTLKTQRRKLTQYQKLDVIEREVEVARELLKKKKDRALLTLRRKKAQEELLKKVDV
CHMP6_NP_078867.2	AILQLKQQRDKLRQYQKRIAQQLEERALARQLLRGRKERAKLLKKKKRYQEQLLDRTEN
Vps20_NP_013794.1	AILEVKRSKDEIHKFTRRTDNLILVEKSQKDLIRKSNMKVRFLKRIHYQEHLQQASD
MpSNF7A_Mp6g10770.1	FQLRIHDQMIMLEGAKATTETVDALRSGASAMKNMQKATNIDDDVKTMDEINEQTEIQIE
AtSNF7-2_At4g29160.1	FQLRIHDQMIMLEGAKATTETVDALRSGASAMKAMQKATNIDDDVKTMDEINEQTEIQIE
AtSNF7-1_At2g19830.1	FQLRIHDQMIMLEGAKATTETVDALRTGASAMKAMQKATNIDDDVKTMDEINEQTEIQIE
MpSNF7B_Mp3g16320.1	YQLRLHDQMILLEGAKATTDVDALRSGAVAMKAIQKQTNIIDVDRTMEDISEQQDQIQD
CHMP4A_NP_054888.3	TLSTLEFQREAIENATTNAEVLRTMELAAQSMKKAYQDMDIDKVDELMTDITEQQEQISD
CHMP4B_NP_789782.1	TLSTIEFQREALENANTNTEVLKNMGYAAKAMKAAHDNMDIDKVDELMQDIADQQEEIST
CHMP4C_NP_689497.1	TLSTIEFQREALENSHTNTEVLNRNMGFAAKAMKSVHENMDLNKIDDLMQEITEQQDEISE
Snf7_NP_013125.1	TMESMEQQQLFSIESANLNLETMRAMQEGAKAMKTIHSGLDIDKVDETMDEIREQVEEISD
AtVPS20-1_AT5G63880.2	WVINVEQQQLTDIELTSKQKAVFESLQKQNSAIKAIQSELDLDDVQKLMDDTADAKAELNA
AtVPS20-2_AT5G09260.1	WLINVEQQQLADIELTSKQKAVFESLQKQNNAIKAIQSEVNLDDVQKLMDDTAEAKAELSA
MpVPS20_Mp5g18760.1	WILNVEQQQLSDIEITSRQKAVFESLQSGHKAIQDLQKEVNIEDVQKLMEDSAEAKAEINA
CHMP6_NP_078867.2	QISSLEAMVQSIEFTQIEMKVMGELQFGNECLNKMHVMSIEEVERILDETQEAVEQIDE
Vps20_NP_013794.1	QLINLENMVSTLEFKMVEKQFINGLNKGNEILKKLNKEFS--NVDELMDDDVQDQIAEINE
MpSNF7A_Mp6g10770.1	ALSTPIGDFDDDELEAELEEELEGAEI
AtSNF7-2_At4g29160.1	ALATPMGDFDEDELAELDELESEEL
AtSNF7-1_At2g19830.1	ALSAPFGDFDEDELEAELEDELEGAEI
MpSNF7B_Mp3g16320.1	ALAAPVGDFDDDELEAELEEELEGTDL
CHMP4A_NP_054888.3	AISRPMGDVDEDELLEEELEEELEQEEL
CHMP4B_NP_789782.1	AISKPVGEFDEDELMAELEELEQEEL
CHMP4C_NP_689497.1	AFSQRVGDFDEDELMAELEELEQEEL
Snf7_NP_013125.1	AISRPLIEVDEDELDEELDMLAQENA
AtVPS20-1_AT5G63880.2	ILGEKL-AEDEEDILAEFDNLESQLI
AtVPS20-2_AT5G09260.1	ILGEKL-AEDEEEILAEFDNLESLLI
MpVPS20_Mp5g18760.1	VLGQQL-DEDDAEVLAELDELETEME
CHMP6_NP_078867.2	LLAGSF-QEDEDAILEELSAITQEIQI
Vps20_NP_013794.1	TLRSRLVSNYEDDLKELDALESELN

Fig. S7. Alignment of SNF7 and VPS20 proteins.

MpVPS24_Mp2g20680.1	NIDRQIRDIQREEKNVKKSIKDAAKRNDMTSAKSLARELVSARRVNVNRLYENRAQLNSVS
AtVPS24-1_At5g22950.1	NIERQIRDIQKEERNVQKAIKEAAKRNDMVSALAKEIVSSRRRTVNRLYENKAQMNSIS
AtVPS24-2_At3g45000.1	TIKSLSDIEREERNVHKAIKDSVKRNDLVTAKALAREIVSSRRRTVKRLYENKAQVNSIS
CHMP3_NP_057163.1	VVDRQIRDIQREEEKVKRSVKDAAKKGQKDCIVLAKEMIRSRKAVSKLYASKAHMNSVL
Vps24_NP_012883.1	NIEKSLRELTVLQNKTTQQLIKKSAAKNDVRTVRLYAKELYQINKQYDRMYTSRAQLDSVR
MpVPS2a_Mp8g06820.1	EIERERQSLQAQEKKLITEIKKTAKQGQMGAVRVMADKLIRTRHQITKFYGLKSQQLQGV
AtVPS2.1_At2g06530.1	EIERERQGLQTQEKKLINTEIKKTAKQGQMGAVRVMADKLIRTRHQIEKFYGLKSQQLQGV
CHMP2A_NP_055268.1	ELDRERQKLETQEKKIADIKKMAKQGQMDAVRIMADKLVRTRRYVRKFVLMRANIQA
Vps2_NP_012924.2	ELEREKRKLELQDKKLVEIKKSAAKNGQVAAAKVQAKDLVRTRNYIQKFDNMKAQLQAIS
MpVPS2c_Mp5g06990.1	GIEREIGTLQLEEKLVAEIKKTAKTGNEAATKILARQLIRLRQQIAKLQGSRAQMGRVA
AtVPS2.3_At1g03950.1	GIEKEIGSLQSEEKLVLEIKRTAKSGNEGATKILARQLIRLRQQIANLQGSRAQMGRGIA
AtVPS2.2_At5g44560.1	GIEREITSLQLEEKRLVAEIKKTAKTGNEAATKILARQLVRLRQQITNLQGSRAQIRGVT
MpVPS2b_Mp1g27870.1	EIEREKQSLHTIETKLIQEIKKAAKVNQWDVAKIMTVDLIRTRQRIIRCYNLYQQLKSIS
MpVPS24_Mp2g20680.1	MHLGESVATVKAUGHQKSTEVMMKLVNGLLKAPEVAATMQELSKEMMKSGVVEEMVSDTL
AtVPS24-1_At5g22950.1	MHLGESVAIARTVGHLSKSAEVMKLVNNLMKAPQMAATMQEFSKEMTKAGVIEEFVNEAI
AtVPS24-2_At3g45000.1	MHLGESIATAVTVGNLSKSGEVMKLVNSLMKAPEIAVTMQAFSKEMTKTGVEEFVSDAV
CHMP3_NP_057163.1	MGMKNQLAVLRVAGSLQKSTEVMMKAMQSLVKIPEIQATMRELSKEMMKAGIIEEMLEDTF
Vps24_NP_012883.1	MKIDEAIRMNTLSNQMADESAGLMREVNLSVRLPQLRNTMIELEKELMKSGIISEMVD
MpVPS2a_Mp8g06820.1	LRIVTLKSTQAMGEAMKGVTKAMGQMNKQLNLPALQNIQEFERQNERMEMTTEVIGDAI
AtVPS2.1_At2g06530.1	LRIQTLKSTQAMGEAMKGVTKAMGQMNRMNLPQLKIMQEFERQNEKMEMVSEVMGDAI
CHMP2A_NP_055268.1	LKIQTLKSNNMAQAMKGVTKAMGTMMNRQLKLPQIQKIMMEFERQAEIMDMKEEMMND
Vps2_NP_012924.2	LRIQAVRSSDQMTSRMSEATGLLAGMNRMTNLPQLQRISMEFEKQSDLMGQRQEFMD
MpVPS2c_Mp5g06990.1	THTQAMYANTAVAGAMKASKAMAAMNKQMEPAKQAKVMQEFQRQSAQMDMTTEMMSDS
AtVPS2.3_At1g03950.1	THTQAMHAHTSVAAGMQGATKAMAAMSKNMDPAKQAKVMREFQKQSAQMDMTTEMMSDS
AtVPS2.2_At5g44560.1	THTQALYASTSISSGMKGATKAMVAMNKQMAPTKQAKVIKDFQKQSAQLDMTIEMMS
MpVPS2b_Mp1g27870.1	LHTQTLKSAESMADVLQGFQKAVRQLNLHVNPALQKIMQEFVHQMRRMDMSLEEMEE--
MpVPS24_Mp2g20680.1	DSALDEIEDEVEKVLLEIAGETIAQLPATALRRLANVR
AtVPS24-1_At5g22950.1	DNALDEIDEEVDKVLTAIAGETAALPVAVIRARLAKVR
AtVPS24-2_At3g45000.1	DNALDEIEEEVDKVLTAIAGETAALPEAVIRYRLANVR
CHMP3_NP_057163.1	ESMDDEAEMEIDRILFEITAGALGKAPSKVMQSRLATLR
Vps24_NP_012883.1	ESVGDAVDEEVNKIVEQYTNEKFKNVQVPMRERLRALQ
MpVPS2a_Mp8g06820.1	DDALEETDELVSQVLDEIGVDLDAQLVTAPLQARLDNLR
AtVPS2.1_At2g06530.1	DDALEETDELVSQVLDEIGIDINQELVNAPLQARLDNLR
CHMP2A_NP_055268.1	DDAMGESDAVVSQVLDELGLSLTDELSNLPLEERLKNLR
Vps2_NP_012924.2	DNVMGEADEIVNKVLDEIGVDLNSQLQSTPLQARLNTLK
MpVPS2c_Mp5g06990.1	DDALDETEELTQQVLDEIGIDIAAQLSSAPLEERLAALR
AtVPS2.3_At1g03950.1	DDALDETEELTNQVLDEIGIDIASQLSSAPLEKRLAALR
AtVPS2.2_At5g44560.1	DETLEDTEELTNQVLDEIGVGVASQLSSAPLEKRLASLR
MpVPS2b_Mp1g27870.1	EDLYEESEQLVQVLDELGVDFSILLNHAPLRDRMNRRLR

Fig. S8. Alignment of VPS24 and VPS2 proteins.

Table. S1. List of primers used in this study

primers	sequences
MpDUO1proFw	CACCGGAAAATTTTGTAGATGATTATAATTGGTATG
MpDUO1proRv	TTTTTATCTGAGACCAGCCACTCCG
MpDUO1proRv_SmaI	CCCGGGTTTTTATCTGAGACCAGCCACTCCG
CitrineFw_SmaI_DUO1pro	CTCAGATAAAAACCCATGGTGAGCAAGGGCGAGGA
Citrine-stopRv_SmaI	GCGCCACCCCTTCCCGCTTCTCCTCCCTTGTACAGCTCGTCCATGC
MpDUO1proFw_HindIII	GGCCAGTGCCAAGCTGGAATAATTTTGTAGATGATTATAATTGGTATG
MpDUO1proRv_HindIII	TTTGTACAAACTTGTTTTTTATCTGAGACCAGCCACTCCG
CitrineRv_HindIII	TTTGTACAAACTTGTCTTGTACAGCTCGTCCATGCCG
MpIFT52proFw	CACCGGTAAACATCCGATAGATTTGTGGAAG
MpIFT52proRv	CTCTTAGAATGGATGCGCATGC
MpIFT52proRv_SmaI	CCCGGGCTCTTAGAATGGATGCGCATGC
CitrineFw_SmaI_IFT52pro	CCATTCTAAGAGCCCATGGTGAGCAAGGGCGAGGA
MpIFT52proFw_HindIII	GGCCAGTGCCAAGCTGGTTAACATCCGATAGATTTGTGGAAG
MpIFT52proRv_HindIII	TTTGTACAAACTTGTCTCTTAGAATGGATGCGCATGC
MpCEN1proFw	CACCACCAGATGAAACCGAGTCCGTGAG
MpCEN1proRv_SmaI	CCCGGGGGTGGAATCGAACGATGACACAGG
CitrineFw_SmaI_CEN1pro	TTCGATTCCACCCCCATGGTGAGCAAGGGCGAGGA
MpCEN1proFw_HindIII	GGCCAGTGCCAAGCTACCAGATGAAACCGAGTCCGTGAG
MpCEN1proRv_HindIII	TTTGTACAAACTTGTGGTGGAATCGAACGATGACACA
MpSNF7aFw	CACCATGTTTCGCTCGGATTTTCGGGAAAC
MpSNF7aRv	TAGAGCCATCTCGGCTTGTAGG
MpVPS24Fw	CACCATGGAAAAGGTTATGGCTTTGATC
MpVPS24_1-152Rv	TGAATCCAGAGTATCGCTCACC
MpVPS2aFw	CACCATGAGCTTCCTTTTTGGGAAGAAG
MpVPS2aRv	TCCGCTTCCTCCCATTTTCCTAAGGTTGTCTAATC
GFPFw_SNF7aScI	GCTCTAAAGGGTGGGATGGTGAGCAAGGGCGAGG
GFPFw_VPS24_1-152AscI	GATTCAAAGGGTGGGGTGAGCAAGGGCGAGG
GFPFw_VPS2aScI	AGCGGAAAGGGTGGGGTGAGCAAGGGCGAGGAGC
GFPRv_AscI	AGCTGGGTCGGCGCGTTACTTGTACAGCTCGTCCATGCCG

Table S2. List of genes used in phylogenetic analysis

genes	species	databases	geneIDs
MpVPS20	<i>Marchantia polymorpha</i>	MarpolBase (v5.1)	Mp5g18760.1
MpSNF7a	<i>Marchantia polymorpha</i>	MarpolBase (v5.1)	Mp6g10770.1
MpSNF7b	<i>Marchantia polymorpha</i>	MarpolBase (v5.1)	Mp3g16320.1
MpVPS24	<i>Marchantia polymorpha</i>	MarpolBase (v5.1)	Mp2g20680.1
MpVPS2a	<i>Marchantia polymorpha</i>	MarpolBase (v5.1)	Mp8g06820.1
MpVPS2b	<i>Marchantia polymorpha</i>	MarpolBase (v5.1)	Mp1g27870.1
MpVPS2c	<i>Marchantia polymorpha</i>	MarpolBase (v5.1)	Mp5g06990.1
AtVPS20-1	<i>Arabidopsis thaliana</i>	TAIR (v11)	AT5G63880.2
AtVPS20-2	<i>Arabidopsis thaliana</i>	TAIR (v11)	AT5G09260.1
AtSNF7-1	<i>Arabidopsis thaliana</i>	TAIR (v11)	At2g19830.1
AtSNF7-2	<i>Arabidopsis thaliana</i>	TAIR (v11)	At4g29160.1
AtVPS24-1	<i>Arabidopsis thaliana</i>	TAIR (v11)	At5g22950.1
AtVPS24-2	<i>Arabidopsis thaliana</i>	TAIR (v11)	At3g45000.1
AtVPS2.1	<i>Arabidopsis thaliana</i>	TAIR (v11)	At2g06530.1
AtVPS2.2	<i>Arabidopsis thaliana</i>	TAIR (v11)	At5g44560.1
AtVPS2.3	<i>Arabidopsis thaliana</i>	TAIR (v11)	At1g03950.1
CHMP6	<i>Homo sapiens</i>	NCBI	NP_078867.2
CHMP4A	<i>Homo sapiens</i>	NCBI	NP_054888.3
CHMP4B	<i>Homo sapiens</i>	NCBI	NP_789782.1
CHMP4C	<i>Homo sapiens</i>	NCBI	NP_689497.1
CHMP3	<i>Homo sapiens</i>	NCBI	NP_057163.1
CHMP2A	<i>Homo sapiens</i>	NCBI	NP_055268.1
Vps20	<i>Saccharomyces cerevisiae</i>	NCBI	NP_013794.1
Snf7	<i>Saccharomyces cerevisiae</i>	NCBI	NP_013125.1
Vps24	<i>Saccharomyces cerevisiae</i>	NCBI	NP_012883.1
Vps2	<i>Saccharomyces cerevisiae</i>	NCBI	NP_012924.2

Table S3. List of accession numbers of genes used in this study.

Gene names	Gene IDs (MpGene IDs)
MpSYP12A	Mp6g00050
MpVAMP71	Mp8g00880
MpSYP2	Mp8g15260
MpDUO1	Mp1g13010
MpCEN1	Mp1g00710
MpIFT52	Mp6g13200
MpGOS11	Mp1g19070
MpSFT1	Mp3g06390
MpSEC22	Mp2g11050
MpSNF7a	Mp6g10770
MpSNF7b	Mp3g16320
MpVPS24	Mp2g20680
MpVPS2a	Mp8g06820
MpVPS2b	Mp1g27870
MpVPS2c	Mp5g06990



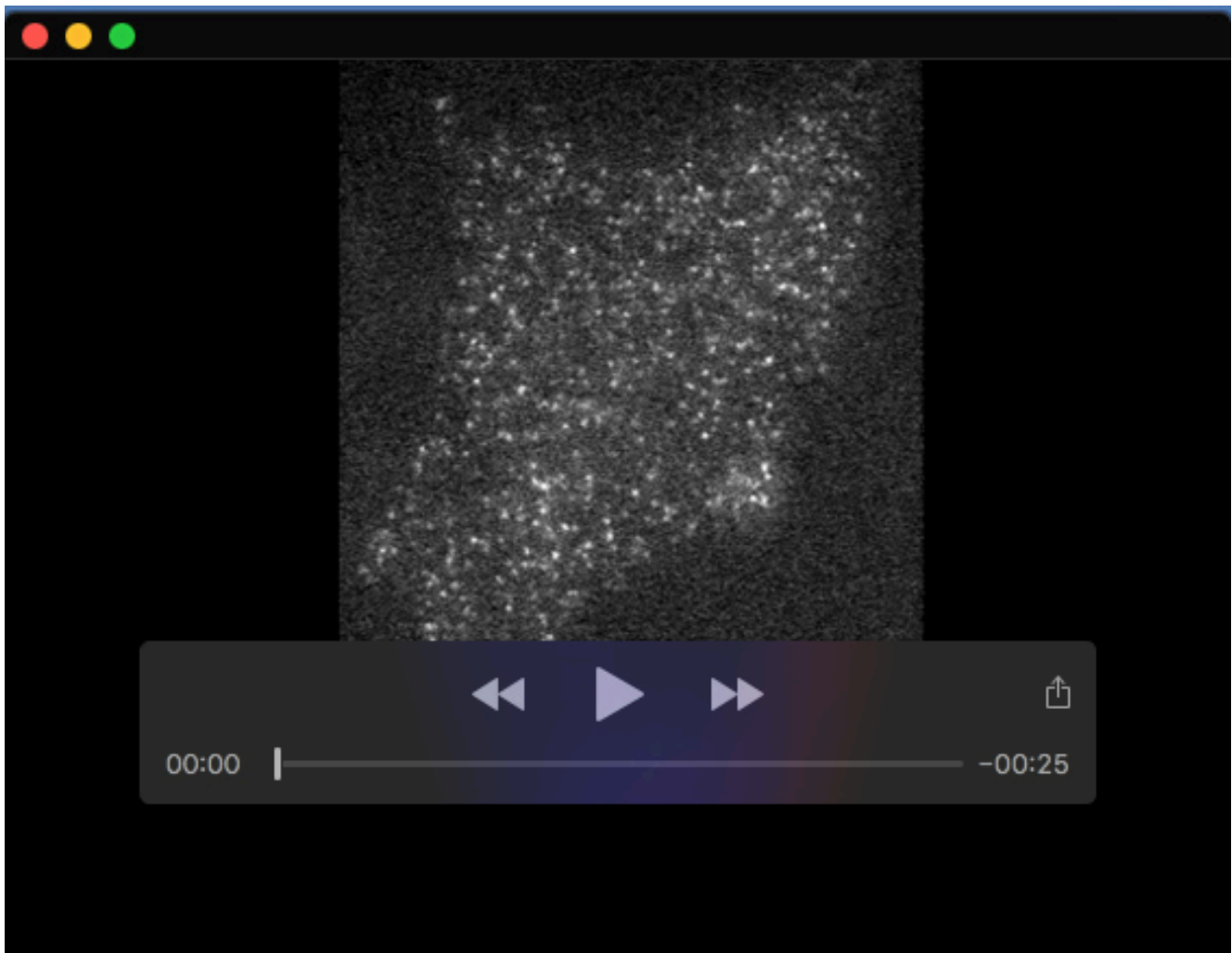
Movie 1. Spermatozooids collected from the line expressing mGFP under regulation of the *MpDUO1* promoter.



Movie 2. Spermatozooids collected from the line expressing MpSNF7a-mGFP under regulation of the MpDUO1 promoter.



Movie 3. Spermatozooids collected from the line expressing MpVPS24¹⁻¹⁵²-mGFP under regulation of the MpDUO1 promoter.



Movie 4. Spermatozooids collected from the line expressing MpVPS2a-mGFP under regulation of the MpDUO1 promoter.

Reference

Leung, K. F., Dacks, J. B. and Field, M. C. (2008). Evolution of the Multivesicular body ESCRT machinery; retention across the eukaryotic lineage. *Traffic* **9**, 1698-1716, doi: 10.1111/j.1600-0854.2008.00797.x.